Undercut and Overhang Angle Control in Topology Optimization: a Density Gradient based Integral Approach

Xiaoping Qian
qian@engr.wisc.edu

Department of Mechanical Engineering
University of Wisconsin-Madison
Madison, WI 53706 - 1572

Abstract We present an approach for controlling the undercut and the minimal overhang angle in density based topology optimization, which are useful for reducing support structures in additive manufacturing. We cast both the undercut control and the minimal overhang angle control that are inherently constraints on the boundary shape into a domain integral of Heaviside projected density gradient. Such a Heaviside projection based integral of density gradient leads to a single constraint for controlling the undercut or controlling the overhang angle in the optimization. It effectively corresponds to a constraint on the projected perimeter that has undercut or has slope smaller than the prescribed overhang angle. In order to prevent trivial solutions of intermediate density to satisfy the density gradient constraints, a constraint on density grayness is also incorporated into the formulations. Numerical results on MBB beams, cantilever beams, and 2D and 3D heat conduction problems demonstrate the proposed formulations are effective in controlling the undercut and the minimal overhang angle in the optimized designs.

Keywords Topology optimization, additive manufacturing, support structure, overhang angle, manufacturability

1 Introduction

Additive manufacturing builds part by depositing materials layer-by-layer under computer control. It has the advantage of building parts of complex shape without part-specific tooling or fixturing. For shape with undercuts, sacrificial support structures are usually used to hold the subsequent layers. The fabrication of such support structures leads to the waste of the materials, build time and energy. Removing support structures can be tedious and

laborious for some additive processes and can lead to the deterioration of surface quality where the support structure meets the part. Many techniques have been developed to reduce the support structures, including finding optimal build directions to reduce the volume of the support structures and designing lattice and cellular support structures to reduce the materials for the support structures. However, thus far, limited research has been done in reducing support structures in the part design stage.

Topology optimization is a computational design method for optimally distributing materials in a design domain under governing physics. It originated as a structural optimization method [1] and has since been applied in problems in fluids, heat transfer, electromagnetic and multiphysics applications [2, 3]. Various methods for topology optimization have been developed. They include density distribution [4, 5, 6], level set [7, 8], topological derivative [9, 10], phase field [11], and evolutionary methods [12]. Incorporating traditional manufacturability constraints into topology optimization has been conducted for some time [13]. Recent work also includes density based explicit constraint for casting [14], projection based constraint for milling [15], and level set based directional constraint in casting [16, 17]. Substantial work has been done in controlling the minimal thickness of topology optimized features [18, 19, 20, 21, 22] and maximal length scale [23, 24, 25]. Method for incorporating fabrication cost in AM has also been developed [26].

In the context of additive manufacturing, reducing the support structure volume or controlling the overhang angle so the part can self-support is desirable. However, little work has been done in considering the influence of support structures in topology optimization. Brackett *et al* highlighted in 2011 [27] the need for considering support structures in topology optimization of parts. Recently maximum overhang angle in topology optimization is considered in [28, 29], using modified projection in the optimization scheme. A layerwise filtering scheme was developed in [30] for designing self-supporting structures. Support structure sensitivity based topology optimization is studied in [31].

In this paper, we develop a density gradient based approach to controlling the undercut and controlling the minimal overhang angle in topology optimization. We adopt the density based approach to topology optimization. Figure 1(a) shows a build direction $\mathbf{b}$ (a normalized vector in this paper) and density gradient $\nabla\gamma$ along the structural boundary. When the dot product of the two directions is larger than zero, it corresponds to undercut. The angle between the two directions forms the overhang angle at the boundary point. When the minimal overhang angle of a structure is larger than a certain prescribed angle $\bar{\alpha}$, the design can self-support, i.e. the support structure is not needed to fabricate the design.

The fundamental challenges in accounting for support structures in topology optimization are how to formulate the support structures into a geometric constraint while the shape and topology of the design is not known *a priori* during the optimization process. Further, such a constraint should be amenable to efficient computation since many iterations are involved in a typical topology optimization process, and the constraint should be differentiable with respect to optimization variables since topology optimization usually employs a gradient based approach due to the heavy expense of finite element solutions of partial differential equations.

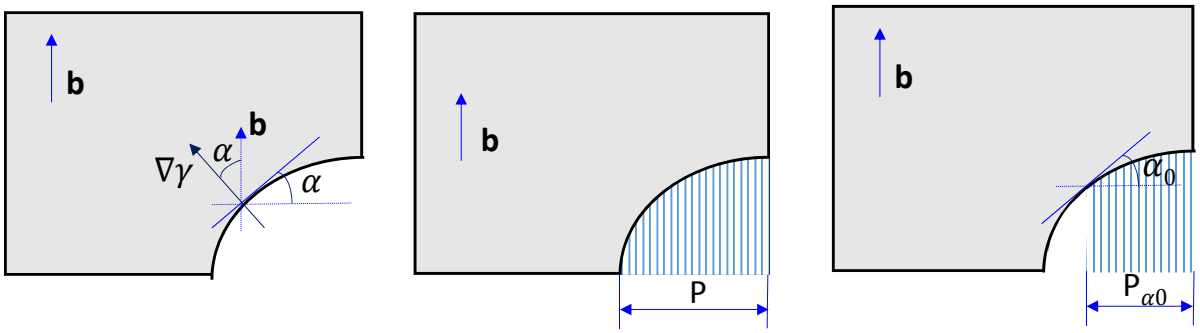

(a) Overhang angle α (b) Projected undercut perimeter P (c) Projected perimeter P_{α_0}

Figure 1: A part with an overhang surface requires support structure for the build direction **b**. (a) Overhang angle α. (b) Support structure characterized by the projected undercut perimeter P. (c) Support structure characterized by the projected perimeter for boundary with overhang angle smaller than α_0.

It is clear from Fig. 1(a) that such undercut or overhang angle can be controlled via constraints on the boundary slope. Instead of directly imposing constraints on the boundary slope which would require explicit knowledge of the boundary, in this paper, we propose to constrain the directional gradient of the density field volumetrically so that *a priori* knowledge of the boundary shape is not needed. We take advantage of the fact that, for a clean design with 0/1 density transition at the boundary, the gradient vanishes in the interior of the domain. Thus the directional gradient constraint can be imposed throughout the domain. In order to efficiently constrain such density gradient across every point in the design domain, we cast it into a single constraint through a Heaviside Projection based Integral (HPI) formulation. The resulting volumetric expressions for constraining the undercut and for constraining the overhang angle are HPI based single functions. They are differentiable and thus can be applied in gradient-based optimization.

We also show that such HPI based expressions geometrically correspond to projected undercut perimeter (PUP) and overhang angle based projected perimeter. PUP corresponds to the perimeter length P of boundary with undercut, projected along the build direction **b**, as shown in Fig. 1(b). It represents the projected undercut *length* for 2D designs and projected undercut *area* for 3D designs. As PUP becomes smaller, undercut volume becomes asymptotically smaller. Thus PUP can be effectively used to control the allowed support volume in the optimized design. Figure 1(c) illustrates the projected perimeter P_{α_0} under overhang angle α_0. It represents the projected perimeter of boundary with overhang angle smaller than α_0, with the projection direction along the build direction **b**. That is, this projected perimeter measure P_{α_0} effectively controls the undercut volume that needs support. In order to avoid possible lateral boundary induced undercut, we also use HPI to form a side zone based projected perimeter constraint. When P_{α_0} and the side zone projected perimeter P_{side} become zero, there is no volume that needs support and the design can therefore self-support.

In order to avoid the appearance of near-uniform intermediate density to satisfy the constraints on the density gradient, a density grayness constraint is also imposed in our formulations. Our numerical experiments demonstrate that the combination of HPI based volumetric constraints on density gradient and the grayness constraints are effective in controlling the undercut and controlling the minimal overhang angle in the optimized designs.

In the remainder of this paper, we first briefly introduce the method of constraining a scalar function via the HPI in Section 2. We then present the directional gradient based integral formulations for controlling the undercut and for controlling the overhang angle in Section 3. The sensitivity of newly formulated constraints is shown in Section 4. Comprehensive numerical results of MBB beams, cantilever beams, 2D and 3D heat conduction problems are shown in Section 5. This paper concludes in Section 6.

2 HPI based constraint formulation

In this paper, our methods for controlling the undercut and the overhang angles are based on formulations that cast these constraints into the form of Heaviside projection based integral. We here briefly describe the Heaviside function and how it can be used to enforce the relation $f(x) \leq \bar{f}$ for a scalar function $f(x)$ over the domain Ω.

A Heaviside function can be defined as follows.

$$H(\xi) = \begin{cases} 1 & \xi > 0, \\ \frac{1}{2} & \xi = 0, \\ 0 & \xi < 0. \end{cases}$$

The specific form of the Heaviside function used in this work is

$$H(\xi) = \frac{1}{1 + e^{-2\beta\xi}}. \tag{1}$$

The Heaviside function value is always non-negative and between 0 and 1. The Heaviside parameter β controls how aggressive the Heaviside function approximates the 0-1 step function. For a moderate Heaviside control parameter β, there exist two critical values ξ_1 and ξ_2 (Fig. 2), where $H(\xi) > 0$ for any $\xi > \xi_1$ and $H(\xi) < 1$ for any $\xi < \xi_2$. A larger β leads to a sharper transition at $\xi = 0$.

We want to ensure that a scalar field function $f(x)$ satisfies the following condition

$$f(x) \leq \bar{f}, \tag{2}$$

where x is in the domain Ω of the function f, $\bar{f}$ is either a fixed scalar value or a scalar function. We can cast it into the following integral form

$$\int_{\Omega} H(f(x) - \bar{f}) \, \mathrm{d}\Omega \leq 0. \tag{3}$$

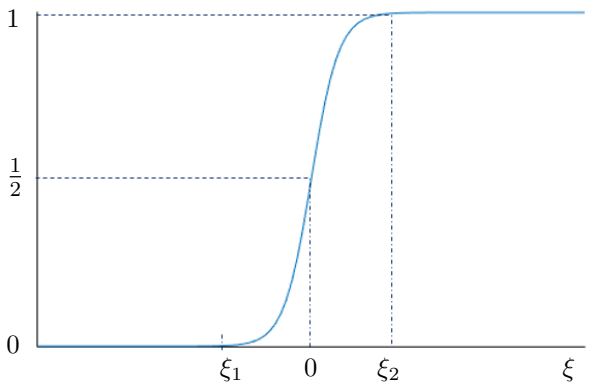

Figure 2: Heaviside function $H(\xi)$.

The equations (2) and (3) are equivalent if the Heaviside function $H(\square)$ is a strict step function. Numerically, there is a transition interval (ξ_1, ξ_2), where the Heavisided function transitions between 0 and 1. Due to the non-negativeness nature of the Heaviside function, (3) is a conservative form of (2) in the sense that any function $f(x)$ satisfies (3), it is guaranteed to satisfy (2). However, the reverse is not true.

3 Directional gradient based integral formulations for controlling the undercut and the minimal overhang angle

In this section, we first give the projected undercut perimeter based formulation for undercut control. We then extend it to generalized projected perimeter based formulation for overhang angle control. Both formulations utilize Heaviside projection based domain integral to constrain the undercut and the overhang angle of the boundary of the underlying designs.

3.1 Projected undercut perimeter based formulation for undercut control

In this subsection, we describe in detail how the HPI form of PUP allows us to characterize the undercut without explicit knowledge of the boundary shape. We describe it in the context of a common minimal compliance problem. Our formulation for topology optimization

considering undercut is as follows

$$\min_{\mathbf{u}\in U,E} \quad C(\mathbf{u}) \qquad \text{Compliance} \tag{4a}$$

$$\text{s.t.} \quad a_E(\mathbf{u},\mathbf{v}) = l(\mathbf{v}), \forall \mathbf{v} \in U_0 \qquad \text{Equilibrium} \tag{4b}$$

$$\frac{\int_\Omega \tilde{\gamma}\ \mathrm{d}\Omega}{\overline{V}} \leq \bar{\theta}, \gamma[0,1] \qquad \text{Volume fraction constraint} \tag{4c}$$

$$\int_\Omega H(\mathbf{b}\cdot\nabla\tilde{\gamma})\mathbf{b}\cdot\nabla\tilde{\gamma}\ \mathrm{d}\Omega \leq \overline{P} \qquad \text{Projected undercut perimeter constraint} \tag{4d}$$

$$\frac{\int_\Omega 4\tilde{\gamma}(1-\tilde{\gamma})\ \mathrm{d}\Omega}{\overline{V}} \leq \bar{\varepsilon} \qquad \text{Density grayness constraint.} \tag{4e}$$

In this formulation, equations (4a), (4b), (4c) form the standard formulation of density based topology optimization for a minimal compliance problem with (4a) as the cost function under an equilibrium constraint (4b) and the volume constraint (4c), where $\mathbf{u}$ is displacement, $\gamma \in [0,1]$ is the optimization variable representing the density before filtering, and $\tilde{\gamma}$ is the filtered density field, $\bar{V}$ represents the volume of the design domain, and $\bar{\theta}$ represents the allowed volume fraction of the material. For density filtering, a Helmholtz partial differential equation (PDE) based filtering is used. The Helmholtz filtering approach [32, 33] is a PDE-based realization of the common density filtering for ensuring length-scale control in topology optimization and it can be conveniently implemented [21, 34] in generic finite element based software such as COMSOL and FEniCS. Isotropic Helmholtz PDE filtering can be described as

$$-r^2\nabla^2\tilde{\gamma} + \tilde{\gamma} = \gamma, \tag{5}$$

where r controls the size of the integral kernel, γ is the input design variable field and $\overline{\gamma}$ is the filtered density. The integral kernel size r in (5) effectively corresponds to $2\sqrt{3}$ times the filter size in the usual density filtering [33].

For topology optimization, we adopt a power law based solid isotropic material with penalization (SIMP) procedure to interpolate material property. The resulting energy bilinear form is noted as

$$a_E(\mathbf{u},\mathbf{v}) = \int_\Omega E(\gamma)\sigma(\mathbf{u}) : \epsilon(\mathbf{v})\ \mathrm{d}x,$$

where $\sigma(\mathbf{u})$ is the stress tensor and $\epsilon(\mathbf{v})$ is the symmetric gradient, and Young's modulus $E(\gamma) = E_{\min} + \tilde{\gamma}^q E_0$. The power coefficient $q = 5$ is used in this work *unless otherwise noted* .

In order to control the amount of undercut, we here add two additional constraints with (4d) constraining the undercut and (4e) constraining the possibly excessive grayness in the density distribution. In (4d) $\overline{P}$ represents the allowed projected undercut perimeter, and $\bar{\varepsilon}$ in (4e) represents the specified grayness measure. Clearly the integral forms of both (4d) and (4e) are easy to compute and differentiate. Now we detail the formulations of these two constraints.

Projected undercut perimeter constraint For convenience, we note the left hand of the PUP constraint (4d) as

$$P \equiv \int_{\Omega} H(\mathbf{b} \cdot \nabla\tilde{\gamma})\mathbf{b} \cdot \nabla\tilde{\gamma} \, \mathrm{d}\Omega, \tag{6}$$

which measures the projected undercut perimeter. In (6), $\mathbf{b}$ is the normalized build direction, $\tilde{\gamma}$ is a density field and $H(\square)$ is the Heaviside function. Equation (6) represents the integration of the directional gradient $\mathbf{b}\cdot\nabla\tilde{\gamma}$ multiplied with the Heaviside function $H(\mathbf{b}\cdot\nabla\tilde{\gamma})$ over the design domain. The term $H(\mathbf{b} \cdot \nabla\tilde{\gamma})$ has the following values

$$H(\mathbf{b} \cdot \nabla\tilde{\gamma}) = \begin{cases} 1 & \mathbf{b} \cdot \nabla\tilde{\gamma} > 0, \\ \frac{1}{2} & \mathbf{b} \cdot \nabla\tilde{\gamma} = 0, \\ 0 & \mathbf{b} \cdot \nabla\tilde{\gamma} < 0. \end{cases}$$

Therefore, (6) represents the integral of the Heavisided directional gradient. Intuitively, equation (6) has contribution only from the boundary for a 0/1 (void/solid) design since density gradient $\nabla\tilde{\gamma}$ vanishes at the interior. As such, the volume integral of directional gradient $\mathbf{b} \cdot \nabla\tilde{\gamma}$ leads to projected perimeter. Due to its 0/1 switch occurring where the density gradient is orthogonal to the build direction $\mathbf{b}$, the use of Heaviside (step) function $H(\mathbf{b} \cdot \nabla\tilde{\gamma})$ thus leads to the measure of projected *undercut* perimeter. When the directional gradient $\mathbf{b}\cdot\nabla\tilde{\gamma}$ is negative at the boundary, i.e. there is no undercut, this term does nothing. When it has undercut, i.e. the directional gradient is positive, it has contribution to the term in (6).

By constraining this term within a pre-specified value, we control the allowed projected undercut perimeter and thus partially constrain the amount of undercut allowed. The geometric meaning of (6) is that it corresponds to the perimeter length of the portion of the boundary with undercut as shown in Fig. 1(b). Therefore, by controlling this term, we control the amount of the perimeter of the boundary with undercut, thus the term undercut perimeter. This undercut perimeter asymptotically represents the amount of undercut volume in the sense. When this undercut perimeter is zero, there would be no undercut. When the undercut perimeter becomes smaller for a given topology, the resulting topology typically has smaller undercut volume. This undercut perimeter does not directly measure the volume of undercut per se, but a simple characterization of the undercut volume.

Grayness constraint The PUP constrains the density gradient, which on its own could lead to optimized designs consisting of intermediate density with zero density gradient. The grayness constraint (4e) is thus imposed to prevent the appearance of such trivial solutions of gray density. In this work, we define the grayness measure as

$$\varepsilon \equiv \frac{\int_{\Omega} 4\tilde{\gamma}(1-\tilde{\gamma}) \, \mathrm{d}\Omega}{\overline{V}}. \tag{7}$$

When $\tilde{\gamma} = 0$ or 1 representing a design that is either completely void or solid, the integrand in (7) vanishes. When $\tilde{\gamma} = 0.5$, the integrand becomes 1. So (7) or the LHS of (4e) give a measure of grayness of the resulting design.

It should be noted that the grayness constraint in and of itself does not restrict the design space since any design with good density contrast and meeting the undercut constraint naturally meets the grayness constraint.

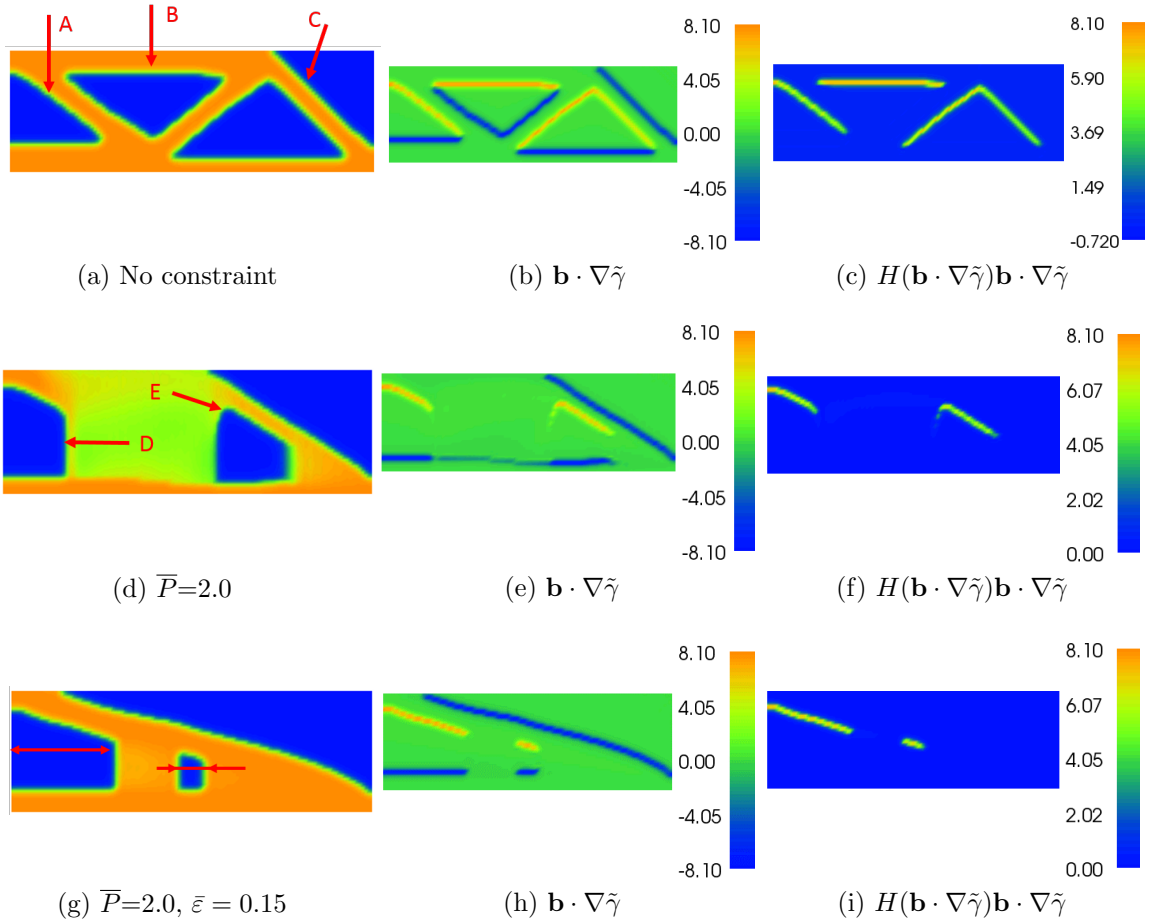

(a) No constraint (b) $\mathbf{b} \cdot \nabla\tilde{\gamma}$ (c) $H(\mathbf{b} \cdot \nabla\tilde{\gamma})\mathbf{b} \cdot \nabla\tilde{\gamma}$

(d) $\overline{P}$=2.0 (e) $\mathbf{b} \cdot \nabla\tilde{\gamma}$ (f) $H(\mathbf{b} \cdot \nabla\tilde{\gamma})\mathbf{b} \cdot \nabla\tilde{\gamma}$

(g) $\overline{P}$=2.0, $\bar{\varepsilon} = 0.15$ (h) $\mathbf{b} \cdot \nabla\tilde{\gamma}$ (i) $H(\mathbf{b} \cdot \nabla\tilde{\gamma})\mathbf{b} \cdot \nabla\tilde{\gamma}$

Figure 3: The proposed method for constraining undercut structures through projected undercut perimeter constraint ($P \leq \overline{P}$) and grayness constraint ($\varepsilon \leq \bar{\varepsilon}$).

Graphical illustration of the two constraints Figure 3 illustrates the essential idea of the proposed formulation: using projected perimeter to control the undercut structure and using grayness measure to suppress intermediate density. In the first row are the optimized design without the projected perimeter constraint or grayness constraint, the corresponding directional gradient of the density, $\mathbf{b} \cdot \nabla\tilde{\gamma}$, along the vertical build direction $\mathbf{b} = (0, 1)$ and the Heavisided directional gradient $H(\mathbf{b} \cdot \nabla\tilde{\gamma})\mathbf{b} \cdot \nabla\tilde{\gamma}$. In the second row are the optimized design with the projected perimeter constraint $\overline{P} = 2.0$ and no grayness constraint, and the

corresponding directional gradient and Heavisided directional gradient. In the third row are the optimized design with projected perimeter constraint $\overline{P} = 2.0$ and grayness constraint $\bar{\varepsilon} = 0.15$, and the corresponding directional gradient and the Heavisided directional gradient. The resulting compliance of the three designs is 208.57, 353.85 and 299.71, respectively. *Note, due to the existence of multiple local minimums, the incorporation of grayness constraint $\bar{\varepsilon} = 0.2$ actually leads to smaller compliance in this particular case.* The detailed parameters for obtaining these designs are available in Section 5.2. This figure suggests the following.

1. *Geometric meaning of Heavisided directional gradient* $H(\mathbf{b} \cdot \nabla\tilde{\gamma})\mathbf{b} \cdot \nabla\tilde{\gamma}$. For a vertical build direction $\mathbf{b}$, location A, B and E in the optimized designs correspond to the boundary with undercut and location C without undercut. Location D has vertical sidewall. This is reflected in the 2nd column of the figure, where undercut regions have positive directional gradient $\mathbf{b} \cdot \nabla\tilde{\gamma}$ and are shown as yellow. On the other hand, in regions without undercut, the directional gradient $\mathbf{b} \cdot \nabla\tilde{\gamma}$ is negative and the regions are shown as blue. Vertical sidewalls corresponds to zero directional gradient. After Heavisiding the directional gradient, only regions with undercuts, i.e. positive directional gradient, retain the directional gradient value and regions without undercuts become zero, as shown in the 3rd column of the figure. The numerical value of $H(\mathbf{b} \cdot \nabla\tilde{\gamma})\mathbf{b} \cdot \nabla\tilde{\gamma}$ corresponds to overhang angle, assuming a clear boundary between the solid and the void. This can be seen by comparing the directional gradient at locations A, B, C, D and E. Location B has highest value in Fig. 11(b) and (c) since it has 90° overhang. Location A and E have smaller value due to the smaller overhang angle. Location D corresponds to a vertical sidewall, thus its boundary does not contribute to the integral of directional gradient.

2. *Geometric meaning of the integral of Heavisided directional gradient as in* (6), $\int_\Omega H(\mathbf{b} \cdot \nabla\tilde{\gamma})\mathbf{b} \cdot \nabla\tilde{\gamma}\ d\Omega$. The integral of such Heavisided directional gradient shown in the third column measures the overall perimeter of the boundary with undercut projected along the build direction, thus the term projected undercut perimeter. Geometrically, the projected perimeter corresponds to integral of the quantities in the third column. For example, for the third design in Fig. 11(g), projected perimeter corresponds to the sum of horizontal length of two boundary segments with undercut. The first design has projected perimeter $P = 6.48$. Both the second and third design meet the projected perimeter constraint, with $P = 2.0$. It is clear that the first design has about three times longer projected perimeter and the second and the third design have the same projected perimeter.

3. *The role of grayness constraint.* Both design two and design three meet the projected perimeter constraint, but the second design has grayness $\varepsilon = 0.43$, a relatively large value due to intermediate density in the middle of the design. The near-uniform distribution of intermediate density between locations D and E leads to low density gradient. This suggests that a projected perimeter constraint alone can lead to designs with near-uniform intermediate density. When the grayness constraint $\bar{\varepsilon} = 0.15$ is imposed as

shown in the third design, the intermediate density disappears. The resulting design has better compliance value than the second one.

3.2 Projected perimeter based formulation for minimal overhang angle control

The formulation in (4) can be extended to a new formulation for minimal overhang angle control as follows

$$
\begin{aligned}
\min_{\mathbf{u}\in U,E} \quad & C(\mathbf{u}) && \text{Compliance} && \text{(8a)}\\
\text{s.t.} \quad & a_E(\mathbf{u},\mathbf{v}) = l(\mathbf{v}), \forall \mathbf{v} \in U_0 && \text{Equilibrium} && \text{(8b)}\\
& \frac{\int_\Omega \bar{\tilde{\gamma}}\ \mathrm{d}\Omega}{\overline{V}} \leq \bar{\theta}, \gamma[0,1] && \text{Volume fraction} && \text{(8c)}\\
& \int_\Omega H_{\bar{\alpha}}\left(\mathbf{b}\cdot\frac{\nabla\bar{\tilde{\gamma}}}{||\nabla\bar{\tilde{\gamma}}||_2}\right)\mathbf{b}\cdot\nabla\bar{\tilde{\gamma}}\ \mathrm{d}\Omega \leq \overline{P}_{\bar{\alpha}} && \text{Projected perimeter} && \text{(8d)}\\
& \frac{\int_\Omega 4\bar{\tilde{\gamma}}(1-\bar{\tilde{\gamma}})\ \mathrm{d}\Omega}{\overline{V}} \leq \bar{\varepsilon} && \text{Density grayness.} && \text{(8e)}
\end{aligned}
$$

The first three equations in this formulation are the cost function (8a), equilibrium constraint (8b) and the volume constraint (8c). The next two equations are similarly the projected perimeter constraint (8d) and density grayness constraint (8e). However, the density field $\bar{\tilde{\gamma}}$ represents the density after density filtering and Heaviside filtering. The projected perimeter now uses a shifted Heaviside function $H_{\bar{\alpha}}(\square)$. We now detail the two differences below.

Heaviside projection of density To alleviate the grayscale transition between the black and white density in the optimized designs, density projection schemes have been used in the past [19, 35, 32]. The goal of the Heaviside projection of density is to use a threshold η to force a density $\tilde{\rho}$ into either solid (1) or void (0). The projected density, also referred to the physical density [20] used in the analysis, $\bar{\tilde{\rho}}_i$, are controlled by two parameters β_d and η. The density projection function can be expressed as

$$
\bar{\tilde{\gamma}} = \begin{cases} \eta[e^{-\beta_d(1-\tilde{\gamma}/\eta)} - (1-\tilde{\gamma}/\eta)e^{-\beta_d}], & (0 \leq \tilde{\gamma} \leq \eta) \\ (1-\eta)[1 - e^{-\beta_d(\tilde{\gamma}-\eta)/(1-\eta)} & \\ \qquad + (\tilde{\gamma}-\eta)/(1-\eta)e^{-\beta_d}] + \eta, & (\eta < \tilde{\gamma} \leq 1) \end{cases} \tag{9}
$$

where the parameter η is the threshold and $\tilde{\gamma}$ is the density field after filtering (5). Density values $\tilde{\gamma}$ larger than η are forced to be 1 in $\bar{\tilde{\rho}}$ and smaller than η are forced to be 0 in $\bar{\tilde{\rho}}$. In this paper, $\eta = 0.5$. The parameter β_d controls the level of aggressiveness in the Heaviside projection of density. This Heaviside projection of density is separate from the Heaviside projection of directional gradient as in (4d) and (8d), where we use a separate parameter β defined in (1) to control the Heaviside projection of density gradient.

It should be noted that both Heaviside projection of density and grayness constraint have the effect of reducing intermediate density. However, their utilities differ in the context of overhang angle control. *The grayness constraint* (8e) *is an integral form. Its effect on controlling the grayness is thus global and it also has the effect of controlling the topology in the resulting design. The density Heaviside density filtering controls the density in a point-wise fashion. More details on the effects of the two techniques are available in Section 5.3.2.*

Overhang angle based Heaviside projection of directional gradient As shown in Fig. 1(c), when the minimal overhang angle α is larger than certain allowed overhang angle $\bar{\alpha}$, the structure can self-support during additive manufacturing processes. That is, a self-supporting boundary satisfies the following

$$\mathbf{b} \cdot \frac{\nabla \bar{\tilde{\gamma}}}{||\nabla \bar{\tilde{\gamma}}||_2} \leq \cos(\bar{\alpha}).$$

We therefore extend the projected perimeter formulation (6) by modifying the Heaviside function so that the 0/1 transition of the Heaviside thresholding occurring at $\cos(\bar{\alpha})$. That is, we impose a Heaviside function at angle $\bar{\alpha}$. We note such a Heavisided function $H_{\bar{\alpha}}$ as

$$H_{\bar{\alpha}}\left(\mathbf{b} \cdot \frac{\nabla \bar{\tilde{\gamma}}}{||\nabla \bar{\tilde{\gamma}}||_2}\right) \equiv H\left(\mathbf{b} \cdot \frac{\nabla \bar{\tilde{\gamma}}}{||\nabla \bar{\tilde{\gamma}}||_2} - \cos(\bar{\alpha})\right) = \begin{cases} 0 & \mathbf{b} \cdot \dfrac{\nabla \gamma}{||\nabla \bar{\tilde{\gamma}}||_2} < \cos(\bar{\alpha}) \\ 0.5 & \mathbf{b} \cdot \dfrac{\nabla \gamma}{||\nabla \bar{\tilde{\gamma}}||_2} = \cos(\bar{\alpha}) \\ 1 & \mathbf{b} \cdot \dfrac{\nabla \gamma}{||\nabla \bar{\tilde{\gamma}}||_2} > \cos(\bar{\alpha}), \end{cases} \tag{10}$$

where the directional gradient $\mathbf{b} \cdot \dfrac{\nabla \bar{\tilde{\gamma}}}{||\nabla \bar{\tilde{\gamma}}||_2}$ is normalized. The new overhang angle based projected perimeter can be represented as

$$P_{\bar{\alpha}} \equiv \int_\Omega H_{\bar{\alpha}}\left(\mathbf{b} \cdot \frac{\nabla \bar{\tilde{\gamma}}}{||\nabla \bar{\tilde{\gamma}}||_2}\right) \mathbf{b} \cdot \nabla \bar{\tilde{\gamma}} \, \mathrm{d}\Omega. \tag{11}$$

In practice, a small value $\bar{P}_{\bar{\alpha}}$ approaching 0 is imposed as a projected perimeter constraint in the RHS of (8d). With this formulation, if the angle from directional gradient of the density is smaller than $\bar{\alpha}$, it contributes to the term $P_{\bar{\alpha}}$ in (11). If the angle is larger than $\bar{\alpha}$, i.e. self-supporting, it does nothing. Therefore, when this constraint is satisfied, there is no directional gradient that has overhang angle smaller than $\bar{\alpha}$. That is, the design self supports.

Figure 4 shows an optimized cantilever design, its directional gradient $\mathbf{b} \cdot \nabla \bar{\tilde{\gamma}}$, normalized directional gradient $\mathbf{b} \cdot \dfrac{\nabla \bar{\tilde{\gamma}}}{||\nabla \bar{\tilde{\gamma}}||_2}$, the Heaviside function $H_{\bar{\alpha}}\left(\mathbf{b} \cdot \dfrac{\nabla \bar{\tilde{\gamma}}}{||\nabla \bar{\tilde{\gamma}}||_2}\right)$, and the directional gradient's projection based on the minimal overhang angle $\bar{\alpha} = 30$, i.e. $H_{\bar{\alpha}}\left(\mathbf{b} \cdot \dfrac{\nabla \bar{\tilde{\gamma}}}{||\nabla \bar{\tilde{\gamma}}||_2}\right) \mathbf{b} \cdot$

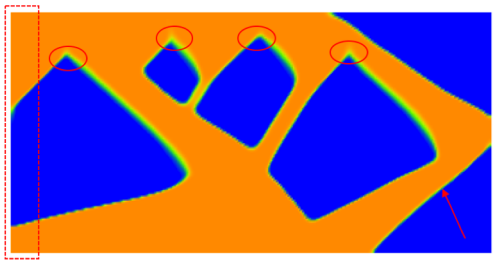

(a) An optimized design

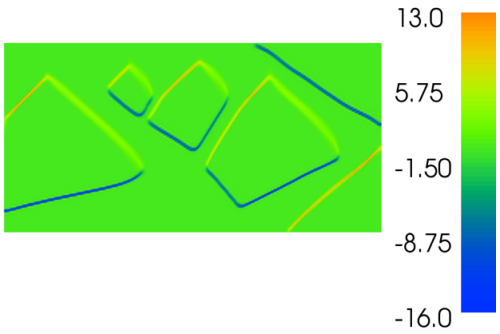

(b) $\mathbf{b} \cdot \nabla\bar{\tilde{\gamma}}$

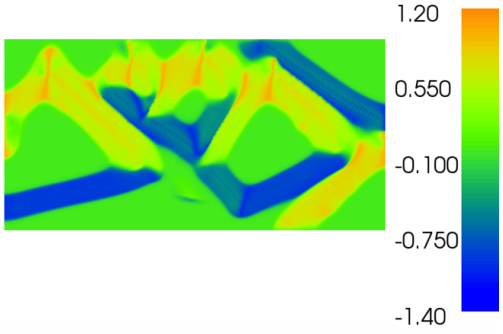

(c) $\mathbf{b} \cdot \dfrac{\nabla\bar{\tilde{\gamma}}}{||\nabla\bar{\tilde{\gamma}}||_2}$

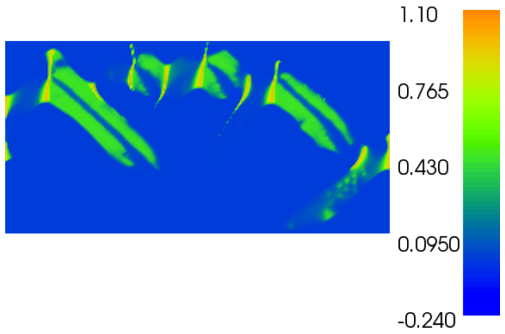

(d) $H_{30^\circ}\left(\mathbf{b} \cdot \dfrac{\nabla\bar{\tilde{\gamma}}}{||\nabla\bar{\tilde{\gamma}}||_2}\right)$

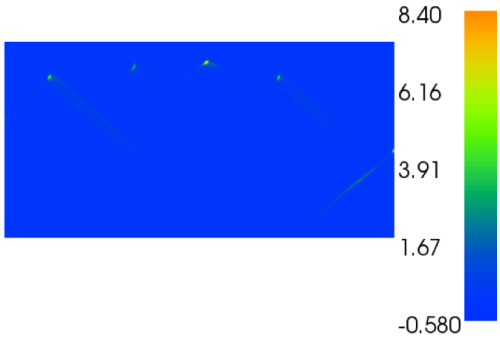

(e) $H_{30^\circ}\left(\mathbf{b} \cdot \dfrac{\nabla\bar{\tilde{\gamma}}}{||\nabla\bar{\tilde{\gamma}}||_2}\right) \mathbf{b} \cdot \nabla\bar{\tilde{\gamma}}$

Figure 4: Directional gradient projected based on minimal overhang angle $\bar{\alpha} = 30$.

$\nabla\bar{\tilde{\gamma}}$. It can be seen that nearly all boundaries disappeared in the Heaviside projected directional gradient plot in Fig. 4(e). Only points circled in Fig. 4(a) appear in 4(e), where the normal of the structural boundary points downward. The boundary edge in the low right part of the design domain as highlighted in Fig. 4(a) appears lightly in 4(e) since its slope is close to 30°. Therefore, when the integral of such projected directional gradient $H_{\bar{\alpha}}\left(\mathbf{b}\cdot\frac{\nabla\bar{\tilde{\gamma}}}{||\nabla\bar{\tilde{\gamma}}||_2}\right)\mathbf{b}\cdot\nabla\bar{\tilde{\gamma}}$ approaches zero, the boundary of the resulting design has no overhang angle smaller than $\bar{\alpha}$ and thus can self-support.

Constraint for side-boundary induced undercut The overhang angle based projected perimeter constraint controls the slope of the boundary in an integral form. However, it may not be effective in obviating the need for support at the lateral sides of the design domain. For example, the design shown in Fig. 4(a) satisfies the overhang angle based projected perimeter constraint. However, the top feature in the dashed region in Fig. 4(a) cannot self-support, even though its slope meets the overhang angle condition. We provide remedy to such side-boundary induced undercut through a constraint, again based on HPI.

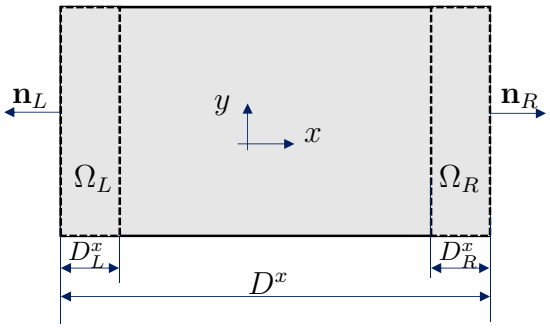

(a) Size zones for imposing side projected perimeter constraint

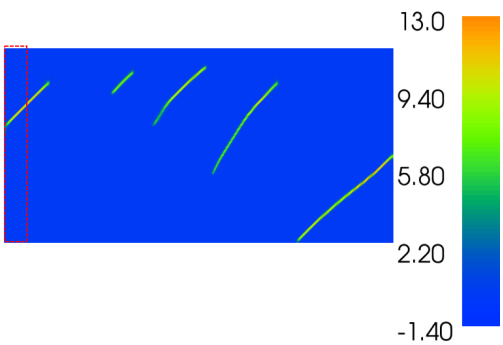

(b) $H(\mathbf{b}\cdot\nabla\bar{\tilde{\gamma}})H(\mathbf{n}_\mathrm{L}\cdot\nabla\bar{\tilde{\gamma}})\mathbf{b}\cdot\nabla\bar{\tilde{\gamma}}$

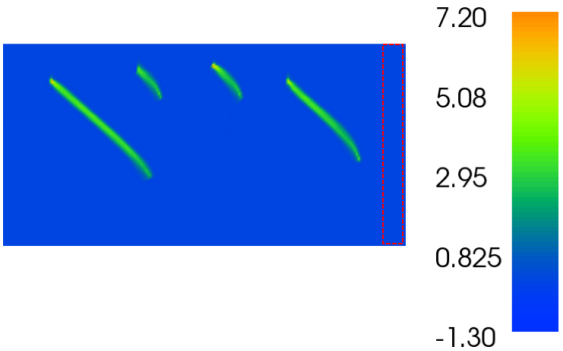

(c) $H(\mathbf{b}\cdot\nabla\bar{\tilde{\gamma}})H(\mathbf{n}_\mathrm{R}\cdot\nabla\bar{\tilde{\gamma}})\mathbf{b}\cdot\nabla\bar{\tilde{\gamma}}$

Figure 5: Side zone constraint for constraining the lateral boundary induced undercut.

In order to prevent such side-boundary induced undercut, we have the following proposition, i.e. a structural feature adjacent to the lateral boundary of the design domain cannot

self-support if and only its density gradient points outward and upward. This enables us to develop the following constraint:

$$\int_{\Omega_{\text{Side}}} H(\mathbf{b}\cdot\nabla\bar{\tilde{\gamma}})H(\mathbf{n}_{\text{side}}\cdot\nabla\bar{\tilde{\gamma}})\mathbf{b}\cdot\nabla\bar{\tilde{\gamma}}\ \mathrm{d}\Omega \le \bar{P}_{\text{Side}} \quad \text{Side projected perimeter,} \tag{12}$$

where Ω_{Side} represents the collection of small zones near the lateral boundary. It should be noted that the normal direction is technically defined only on the domain boundary and not for the interior of the domain. So it is noted as $\mathbf{n}_{\text{side}}$. That is, for each side, there is a small side domain and there is one corresponding normal direction $\mathbf{n}_{\text{side}}$. For three-dimensional problems, multiple lateral size zones can be defined. All these boundary zones are cast into one constraint. Figure 5(a) gives an example where Ω_{Side} is a collection of left side zone Ω_L and right side zone Ω_R. So the LHS of (12) includes the following two terms

$$\int_{\Omega_{\text{L}}} H(\mathbf{b}\cdot\nabla\bar{\tilde{\gamma}})H(\mathbf{n}_{\text{L}}\cdot\nabla\bar{\tilde{\gamma}})\mathbf{b}\cdot\nabla\bar{\tilde{\gamma}}\ \mathrm{d}\Omega + \int_{\Omega_{\text{R}}} H(\mathbf{b}\cdot\nabla\bar{\tilde{\gamma}})H(\mathbf{n}_{\text{R}}\cdot\nabla\bar{\tilde{\gamma}})\mathbf{b}\cdot\nabla\bar{\tilde{\gamma}}\ \mathrm{d}\Omega.$$

This form in (12) is applicable to both 2D and 3D domains. In this constraint, $H(\mathbf{b}\cdot\nabla\bar{\tilde{\gamma}})$ filters out any upward density gradient (i.e. $\mathbf{b}\cdot\nabla\bar{\tilde{\gamma}} < 0$) and $H(\mathbf{n}_{\text{side}}\cdot\nabla\bar{\tilde{\gamma}})$ filters out any inward density gradient, where $\mathbf{n}_{\text{side}}$ represents the outward normal direction of each lateral boundary. Thus the LHS of (12) represents the projected perimeter of the boundary in the side zone that has normal outward and downward. When this perimeter is 0, or in practice a very small value $\bar{P}_{\text{side}}$, the resulting design is free from such undercut induced by the side-boundary. For the design in Fig. 4(a), the two integrands $H(\mathbf{b}\cdot\nabla\bar{\tilde{\gamma}})H(\mathbf{n}_{\text{L}}\cdot\nabla\bar{\tilde{\gamma}})\mathbf{b}\cdot\nabla\bar{\tilde{\gamma}}$ and $H(\mathbf{b}\cdot\nabla\bar{\tilde{\gamma}})H(\mathbf{n}_{\text{R}}\cdot\nabla\bar{\tilde{\gamma}})\mathbf{b}\cdot\nabla\bar{\tilde{\gamma}}$ are plotted in Fig. 5(b) and (c). It can be seen that the region corresponding to the undercut feature requiring support in Fig. 4(a) appears in high intensity in the dashed region in Fig. 5(b). Thus, constraining such projected perimeter in the side zones can avoid lateral boundary induced undercuts.

4 Sensitivity analysis

Our topology optimization uses a gradient based optimization approach. Therefore the sensitivity of the cost function and constraints with respect to optimization variable γ is required. The sensitivity of the cost function (minimal compliance) and the volume constraint are common knowledge within the topology optimization community. We here focus on the sensitivity analysis for the PUP constraint (4d), density grayness constraint (4e), overhang angle based projected perimeter constraint (8d), and side zone based projected perimeter constraint (12).

Our implementation is based on FEniCS [36], an open source finite element package. FEniCS is a class of finite element analysis package that can automatically assemble the weak form of PDEs into discrete stiffness matrix and load vector. Other example of such class of FE software include commercial software COMSOL. So here we provide the variational expressions for the sensitivity of these constraints, from which the sensitivity vector of each

constraint with respect to the nodal optimization variable γ can be obtained automatically through FEniCS. In the following, we note the variation of the nodal optimization variable γ as $\delta\gamma$, the variation of the Helmholtz PDE filtered density as $\delta\tilde{\gamma}$ and the variation of the Heaviside density filtering after the PDE filter as $\delta\bar{\tilde{\gamma}}$. The relationships between $\delta\gamma$, $\delta\tilde{\gamma}$ and $\delta\bar{\tilde{\gamma}}$ can be obtained from differentiation of (5) and (9).

The sensitivity of the PUP constraint (4d) is

$$\int_\Omega H(\mathbf{b}\cdot\nabla\tilde{\gamma})\mathbf{b}\cdot\nabla\delta\tilde{\gamma} + H(\mathbf{b}\cdot\nabla\tilde{\gamma})'\mathbf{b}\cdot\nabla\delta\tilde{\gamma}\mathbf{b}\nabla\tilde{\gamma}\ \mathrm{d}\Omega, \tag{13}$$

where the gradient of the Heaviside function (1) with respect to its argument $\square$ is as follows

$$H'(\square) = \frac{-1}{(1+e^{-2\beta\square})^2}(-2\beta)e^{-2\beta\square}. \tag{14}$$

The sensitivity of the grayness constraint (4e) is

$$\frac{1}{\bar{V}}\int_\Omega 4(1-2\tilde{\gamma})\delta\tilde{\gamma}\ \mathrm{d}\Omega. \tag{15}$$

The sensitivity of the overhang angle based projected perimeter constraint (8d) is

$$\int_\Omega H_{\bar{\alpha}}\left(\mathbf{b}\cdot\frac{\nabla\bar{\tilde{\gamma}}}{||\nabla\bar{\tilde{\gamma}}||_2}\right)\mathbf{b}\cdot\nabla\delta\bar{\tilde{\gamma}}\ \mathrm{d}\Omega + \int_\Omega H_{\bar{\alpha}}(\square)'\left(\mathbf{b}\cdot\frac{\nabla\delta\bar{\tilde{\gamma}}}{||\nabla\bar{\tilde{\gamma}}||_2} - \mathbf{b}\cdot\frac{\nabla\bar{\tilde{\gamma}}}{||\nabla\bar{\tilde{\gamma}}||^{3/2}}\nabla\bar{\tilde{\gamma}}\cdot\nabla\delta\bar{\tilde{\gamma}}\right)\mathbf{b}\cdot\nabla\bar{\tilde{\gamma}}\ \mathrm{d}\Omega \tag{16}$$

where $H_{\bar{\alpha}}(\square)'$ follows (14) with $\square$ representing $\mathbf{b}\cdot\frac{\nabla\bar{\tilde{\gamma}}}{||\nabla\bar{\tilde{\gamma}}||_2}$.

The sensitivity of the side zone projected perimeter constraint (12) is

$$\begin{aligned}\int_{\Omega_{\text{Side}}} &(H(\mathbf{b}\cdot\nabla\bar{\tilde{\gamma}})H(\mathbf{n}_{\text{side}}\cdot\nabla\bar{\tilde{\gamma}})\mathbf{b}\cdot\nabla\delta\bar{\tilde{\gamma}} \\ &+H(\mathbf{b}\cdot\nabla\bar{\tilde{\gamma}})'\mathbf{b}\cdot\nabla\delta\bar{\tilde{\gamma}}H(\mathbf{n}_{\text{side}}\cdot\nabla\bar{\tilde{\gamma}})\mathbf{b}\cdot\nabla\bar{\tilde{\gamma}} \\ &+H(\mathbf{b}\cdot\nabla\bar{\tilde{\gamma}})H(\mathbf{n}_{\text{side}}\cdot\nabla\bar{\tilde{\gamma}})'\mathbf{n}_{\text{side}}\cdot\nabla\delta\bar{\tilde{\gamma}}\mathbf{b}\cdot\nabla\bar{\tilde{\gamma}})\ \mathrm{d}\Omega.\end{aligned} \tag{17}$$

5 Numerical results

We present below our numerical implementation and numerical results for optimized designs with undercut control based on PUP constraints and with minimal overhang angle control based on generalized projected perimeter constraints. Both minimal elastic compliance problems and minimal thermal compliance problems are presented.

5.1 Numerical implementation

The formulations have been implemented based on FEniCS [36]. The optimizer is the method of moving asymptotes [37]. Our formulations essentially involve the computation of two density based quantities: integrals of density gradient as in undercut based PUP (4d), overhang

based PUP (8d) and sidezone perimeter (12), and integral of density as in the grayness measure (4e). In our implementation, we adopt a finite element node based representation of density distribution. Our FE elements are linear triangular elements. Thus the density distribution is piecewise linear and the density gradient is piecewise constant. So both projected perimeter measures based on density gradient and grayness measure based on the density can be calculated through integration of piecewise constant and piecewise linear functions.

Besides the integral quantities such as projected perimeter and grayness measure used in our optimization formulation, it can be useful to visualize point-wise density gradient such as those in figures 3, 4, and 5. In our FE node based density representation, density gradient is piecewise constant. For the ease of visualization, we project such piecewise constant quantities into FE space, i.e. piecewise linear quantities. This way, the projected density gradient can be visualized just as the usual piecewise linear FE solutions. The specific implementation of such projection is through FEniCS [36]. For example, if we are interested in visualizing the discretized, piecewise constant $\mathbf{b} \cdot \frac{\nabla \bar{\tilde{\gamma}}}{|\nabla \bar{\tilde{\gamma}}|_2}$, we seek a piecewise linear FE function $w \in V^h$ to approximate the discrete $\mathbf{b} \cdot \frac{\nabla \bar{\tilde{\gamma}}}{|\nabla \bar{\tilde{\gamma}}|_2}$ where V^h represents the space of the piecewise linear triangular elements. The variational problem for the projection operation reads: find $w \in V^h$ such that

$$a(w, v) = L(v) \quad \forall v \in V_0^h \tag{18}$$

where

$$a(w, v) = \int_\Omega w \cdot v \, \mathrm{d}x,$$
$$L(v) = \int_\Omega \left(\mathbf{b} \cdot \frac{\nabla \bar{\tilde{\gamma}}}{|\nabla \bar{\tilde{\gamma}}|_2} \right) \cdot v \, \mathrm{d}x.$$

The solution to (18) is thus a piecewise linear approximation to the piecewise constant $\mathbf{b} \cdot \frac{\nabla \bar{\tilde{\gamma}}}{|\nabla \bar{\tilde{\gamma}}|_2}$. Thus overshoot or undershoot approximation of $\mathbf{b} \cdot \frac{\nabla \bar{\tilde{\gamma}}}{|\nabla \bar{\tilde{\gamma}}|_2}$ may occur. For example, in Fig. 4(b), the values of $\mathbf{b} \cdot \frac{\nabla \bar{\tilde{\gamma}}}{|\nabla \bar{\tilde{\gamma}}|_2}$ exceeds the expected range $[-1, 1]$. However, such a projection operation is only used for visualizing the density gradient. It is not used in the calculation of either projected perimeters or density grayness.

Although our implementation is based on the FE node based density representation, our formulations are also applicable to other density representations. In the alternative density representation such as element based piecewise constant density representation, the density gradient can be computed through finite difference schemes [2, 38, 39]. In the B-spline based smooth density representation [40], the density gradient can even be computed exactly without approximation.

5.2 PUP based optimized designs for undercut control

In this subsection, we present our numerical results based on optimized designs of MBB beams (2D) and cantilever beam (3D) under various PUP and grayness constraints. The model specifications are displayed in Fig. 6. We first present 2D designs, including the

optimized various MBB beams under different projected perimeter constraints, under different grayness constraints, and under different build directions. The optimized 3D designs are shown in Section 5.2.3. In all examples below, the convergence criteria is the maximum change of nodal density γ should be smaller than 0.01 or the number of iterations reach 350. The Heaviside parameter β in (1) is 2 for all 2D designs.

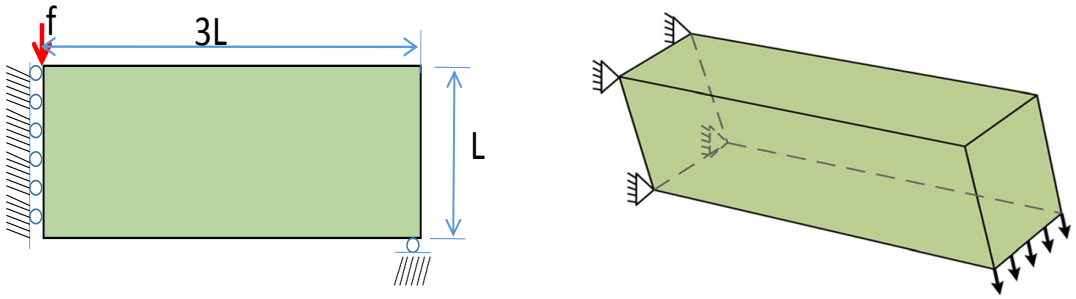

(a) MBB beam (2D) (b) Cantilever beam (3D)

Figure 6: Boundary conditions of MBB beams and cantilever beams

For all the 2D examples, the domain is of size 6×2 and is divided into 9,600 linear triangular elements with 4,961 nodes, where two shorter and orthogonal sides of each triangle element is of size $h = 0.05$. The Young's modulus is 1 for the solid and $1.0e^{-9}$ for the void and the Poisson ratio is 0.3. The Helmholtz filter radius r in the PDE filter (5) is characterized in terms of the number of elements r_f in the usual density filtering, i.e. $r = r_f/(2\sqrt{3}h)$. We have chosen r_f in the PDE filter (5) to be 3. The volume fraction $\bar{\theta}$=0.5 for the 2D examples.

In the numerical examples below, the volume constraints for all designs are active. For projected perimeter and grayness constraints, if only $\overline{P}$ or $\bar{\varepsilon}$ is given, the constraint is active. If either one is inactive, the actual value and the constraint are reported together in a fraction form as $P/\overline{P}$ and $\varepsilon/\bar{\varepsilon}$.

5.2.1 Optimized designs under different projected perimeter and grayness constraints

Figure 7 shows optimized designs under different projected perimeter constraints with $\overline{P}$ ranging from 4.0 to 1.0. The corresponding grayness constraints $\bar{\varepsilon}$ and the compliance of the resulting optimized designs are also listed. These designs demonstrate that, as $\overline{P}$ becomes small, the projected undercut perimeter indeed becomes smaller and the compliance becomes bigger.

Figure 8 displays various designs obtained with projected perimeter constraints ranging from $\overline{P} = 1.0$ to 0.1. In each design, the corresponding grayness constraint and the compliance are also displayed in each subfigure. It can be seen that, as $\overline{P}$ becomes smaller, the projected undercut perimeter indeed becomes smaller and the compliance becomes larger. When $\overline{P}$ is 0.1 in Fig. 8(f), the resulting design has no undercut at all and the projected

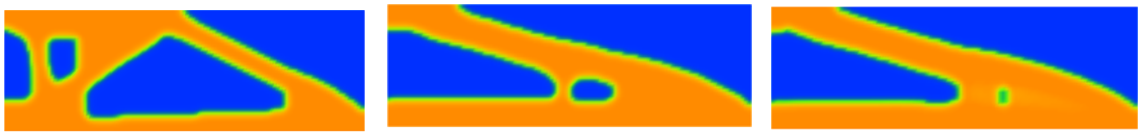

(a) $\overline{P}$=4.0, $\bar{\varepsilon}$=0.175, C=243.95 (b) $P/\overline{P}$=3.27/3.5, $\bar{\varepsilon}$=0.15, C=267.14 (c) $\overline{P}$=3.0, $\bar{\varepsilon}$=0.15, C=269.88

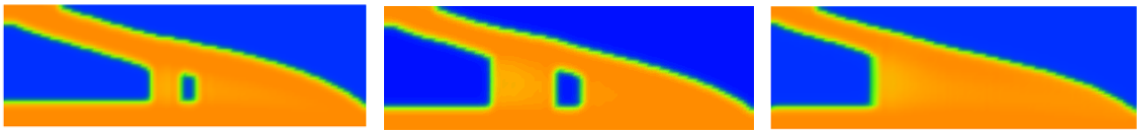

(d) $\overline{P}$=2.5, $\bar{\varepsilon}$=0.15, C=275.23 (e) $\overline{P}$=2, $\bar{\varepsilon}$=0.15, C=299.62 (f) $\overline{P}$=1.5, $\bar{\varepsilon}$=0.15, C=326.31

Figure 7: Optimized MBB beams under different projected perimeter constraints, ranging from $\overline{P}$=4.0 to $\overline{P}$=1.0.

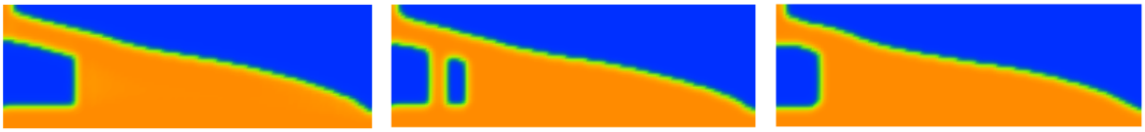

(a) $\overline{P}$=1.0, $\bar{\varepsilon}$=0.12, C=417.89 (b) $\overline{P}$=0.8, $\bar{\varepsilon}$=0.12, C=466.41 (c) $\overline{P}$=0.6, $\bar{\varepsilon}$=0.10, C=493.67

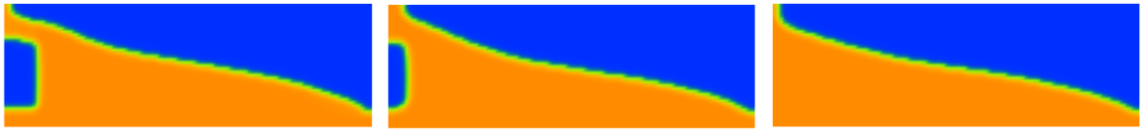

(d) $\overline{P}$=0.4, $\bar{\varepsilon}$=0.10, C=530.57 (e) $\overline{P}$=0.2, $\bar{\varepsilon}$=0.09, C=605.28 (f) $P/\overline{P}$=-0.084/0.1, $\bar{\varepsilon}$=0.075, C=651.08

Figure 8: Optimized MBB beams under different projected perimeter constraints, ranging from $\overline{P}$=1.0 to $\overline{P}$ = 0.1.

undercut perimeter $P = -0.084$. As a general rule of thumb, as projected perimeter constraint becomes smaller, the grayness measure $\bar{\varepsilon}$ also becomes smaller. At the boundary, the intermediate density transitioning between the solid and the void occurs. For designs with larger undercut perimeters, more intermediate density occurs along the boundary and thus a larger grayness measure is desired. Otherwise, a tighter grayness measure would unnecessarily tighten the perimeter and reduce the boundary or the number of holes in the optimized design.

It should be pointed out that the proposed PUP measure only exerts partial control of the perimeter, i.e. the projected perimeter, of the undercut boundary. In this specific example, the build direction **b** is vertical, and the PUP thus effectively controls the horizontal length of the undercut boundary. As the allowed PUP decreases from 1.0 to 0.2, the horizontal length of the undercut area indeed becomes smaller and smaller. When the allowed projected perimeter $\bar{P}$ approaching zero, the resulting design has no undercut as shown in Fig. 8(f). However, the full perimeter of the undercut boundary does not necessarily become smaller as $\bar{P}$ becomes smaller. For example, the design in Fig. 8(b) actually has larger undercut perimeter, considering its perimeter in vertical direction, than that in Fig. 8(a), even though its allowed PUP length is smaller. The perimeter along the uncontrolled direction, i.e. the build direction **b**, is thus varied by the optimizer to minimize the cost function.

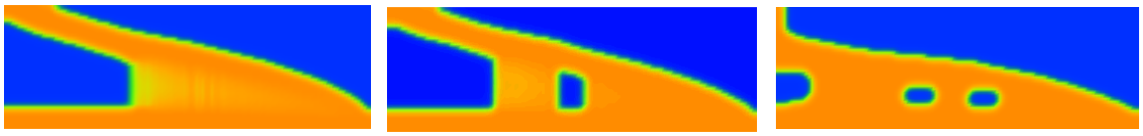

(a) P=2.0, $\varepsilon/\bar{\varepsilon}$=0.16/0.20, C=290.83 (b) P=2.0, $\bar{\varepsilon}$=0.15, C=299.62 (c) P=1.36, $\bar{\varepsilon}$=0.12, C=518.86

Figure 9: Role of grayness constraint $\bar{\varepsilon}$ at $\overline{P}$=2.0.

Figure 9 shows the resulting design under different grayness constraint $\bar{\varepsilon}$ at $\overline{P} = 2.0$. When the constraint $\bar{\varepsilon} = 0.2$, the resulting design contains substantial intermediate density as shown in Fig. 9(a) and the grayness constraint is inactive with grayness $\varepsilon = 0.16$, but the projected perimeter constraint with $P = 2.0$. When the constraint $\bar{\varepsilon} = 0.15$, both the projected perimeter constraint and the grayness constraints are active, i.e. $P = \overline{P} = 2.0$ and $\varepsilon = \bar{\varepsilon} = 0.15$. When the constraint becomes smaller with $\bar{\varepsilon} = 0.12$, the projected perimeter constraint is inactive with $P = 1.36$ and the grayness constraint is active with $\varepsilon = \bar{\varepsilon} = 0.12$. This example suggests, with a large grayness constraint, the design is mostly constrained by the projected perimeter constraint. With a small constraint, the design is constrained by the projected perimeter constraint. For an intermediate grayness constraint, the resulting designs are constrained by both the projected perimeter constraint and the grayness constraint.

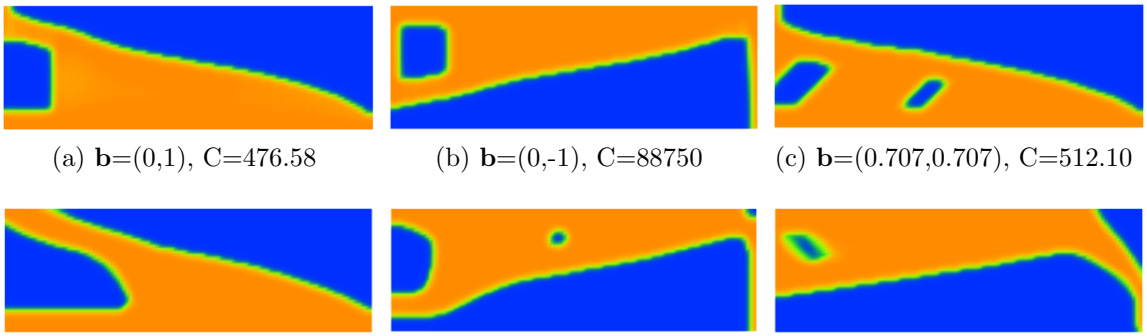

(a) **b**=(0,1), C=476.58 (b) **b**=(0,-1), C=88750 (c) **b**=(0.707,0.707), C=512.10

(d) **b**=(-0.707,0.707), C=315.47 (e) **b**=(-0.707,-0.707), C=636.11 (f) **b**=(0.707,-0.707), C=712.48

Figure 10: Optimized designs under different build directions **b** with $\overline{P} = 0.6$ and $\bar{\varepsilon} = 0.12$.

5.2.2 Optimized designs under different build directions

Figure 10 displays various designs under different build direction **b** and the corresponding compliance C under the projected perimeter constraint $\overline{P} = 0.6$ and grayness constraint $\bar{\varepsilon} = 0.12$. These directions include the default up direction **b**=(0,1), bottom up direction **b**=(0,-1), and 45°, 135°, 225° and 315° with respect to x-axis, respectively. In all cases, the optimized designs are obtained with both the projected perimeter and grayness constraints active. By comparing these designs, we can see that the design in Fig. 10(d) under 135° with $\mathbf{b} = (-0.707, 0.707)$ gives best compliance, under the same projected perimeter constraint. This example suggests that the proposed approach can also be used to select a build direction with better performance under a given support constraint $\overline{P}$.

5.2.3 3D designs under projected perimeter constraints

Figure 11 shows optimized 3D designs under different undercut perimeter constraints. The domain is of size $4 \times 2 \times 2$ and is divided into 96,000 linear tetrahedral elements, consisting of 18,081 nodes. The volume fraction $\bar{\theta}$ is 15% of the design domain. The Young's modulus is 1 for solid and 10^{-9} for the void. The filter size r_f is 3. The primary and adjoint state equations are solved via an iterative solver, successive over-relaxation as a preconditioner in a conjugated gradient iterative solver. All designs are obtained with $\bar{\varepsilon} = 0.2$ and $\beta = 4.0$, except the last two designs. The last two designs are obtained with $\bar{\varepsilon} = 0.15$ and $\beta = 20$. Figure 11(a) shows two views of the optimized design without the projected perimeter constraint and the compliance is 1.448e5. The remaining designs in Fig. 11 correspond to projected perimeter constraint $\overline{P} = 2.0, 1.0, 0.5, 1.0^{-3}$, and 1.0^{-4}, respectively. The corresponding compliances are, respectively, 1.294e5, 1.286e5, 1.400e5, 1.656e5, and 3.583e5. This numerical example suggests the following.

1. As the projected perimeter becomes smaller, the resulting designs have less support volume. In the end, when the projected perimeter becomes close to zero, the resulting designs, Fig. 11(e) and (f), have no undercut. This suggests that the proposed

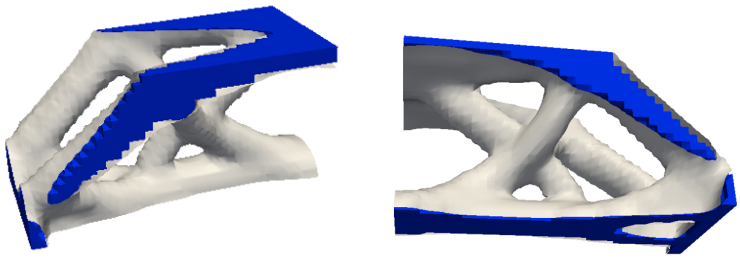

(a) No constraint, $P = 3.647$, C=1.448e5

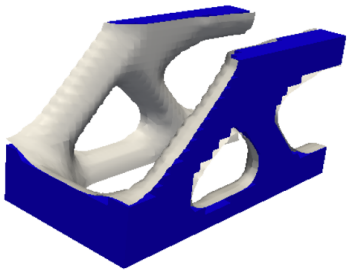

(b) $P/\overline{P}$=1.45/2.0, C=1.294e5

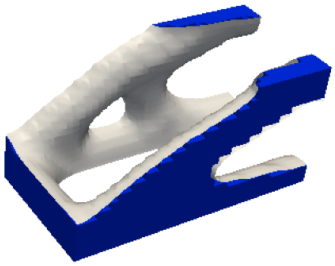

(c) $\overline{P} = 1.0$, C=1.286e5

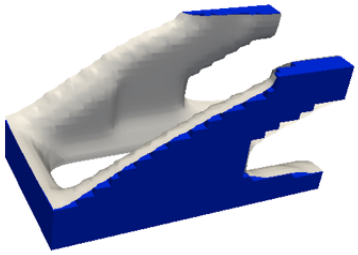

(d) $\overline{P} = 0.5$, C=1.400e5

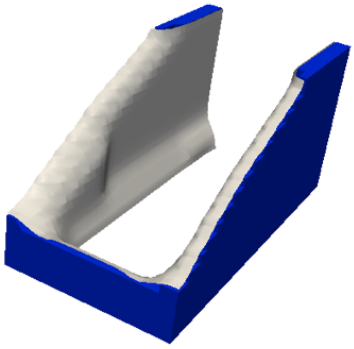

(e) $\overline{P} = 1.0$e-3, C=1.656e5

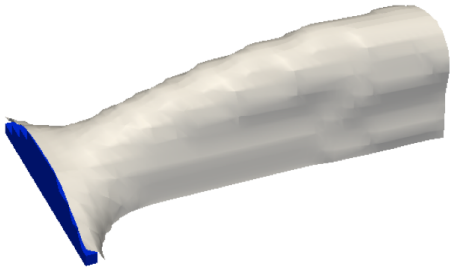

(f) $P/\overline{P}$ =-0.02/1.0e-4, C=3.583e5

Figure 11: 3D minimal compliance optimization under different undercut perimeter constraint $\bar{\varepsilon} = 0.2$.

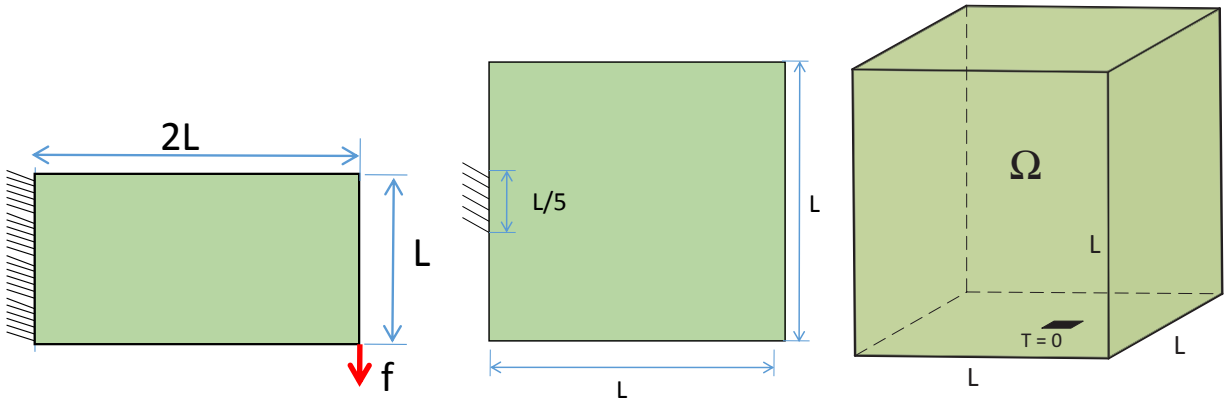

(a) Cantilever beam (b) Heat conduction (2D) (c) Heat conduction (3D)

Figure 12: Boundary conditions for three overhang angle examples.

projected perimeter is an effective measure for controlling the support structures.

2. Unlike all earlier 2D numerical examples, optimized 3D designs with projected perimeter constraint do not necessarily lead to worse compliance since the design in Fig. 11(b), (c), and (d) all have smaller compliance than the design in Fig. 11(a). This can be ascribed to the fact the topology optimization problem in (4) is highly non-convex. The existence of multiple local minimums may preclude an optimizer from reaching a better design. The same phenomenon has been observed in topology optimization under manufacturability constraints in [13, 30].

5.3 Minimal overhang angle control in optimized designs

In this subsection, we present the optimized designs from the formulation (8) that involves the HPI form of projected perimeter constraints for minimal overhang angle control. The examples include 2D cantilever beam designs, 2D and 3D heat conduction examples. Figure 12 displays the boundary conditions for the three examples.

5.3.1 Minimal overhang angle control in optimal design of cantilever beams

We apply this overhang angle control method in the design of a cantilever beam. The design objective is to minimize the compliance. The domain is of size 12×6. This domain is discretized into 57,600 linear triangular elements and 29,161 vertices where two shorter and orthogonal sides of each triangle element is of size $h = 0.05$. The allowed volume fraction $\bar{\theta}$ of the solid material is 0.5. Side projected perimeter constraint (12) is also imposed on side zones to prevent size zone induced undercut. Two side zones on the left and right side of width at 10% of the total width are imposed with the side perimeter constraint $\bar{P}_{\text{side}} = 0.3$. The filter size r_f is 25 in all examples in this section unless otherwise specified. The β for the Heaviside projection of directional gradient in (1) is 10. The β_d in the Heaviside filter

(9) is applied at iteration 49 and doubles every 25 iterations until it reaches $\beta_d^{\max} = 32$. The grayness constraint $\bar{\varepsilon}$ starts with 1.0 and decreases by 50% every 25 iterations until it reaches 0.5 or otherwise specified. *The continuation scheme for adjusting $\beta_d^{\max}$ and $\bar{\varepsilon}$ is used to ensure the smooth convergence of the optimization process. After certain iterations and before the iteration ends, both $\beta_d^{\max}$ and $\bar{\varepsilon}$ would become constant during the iteration process to ensure the consistency of the optimization problem.*

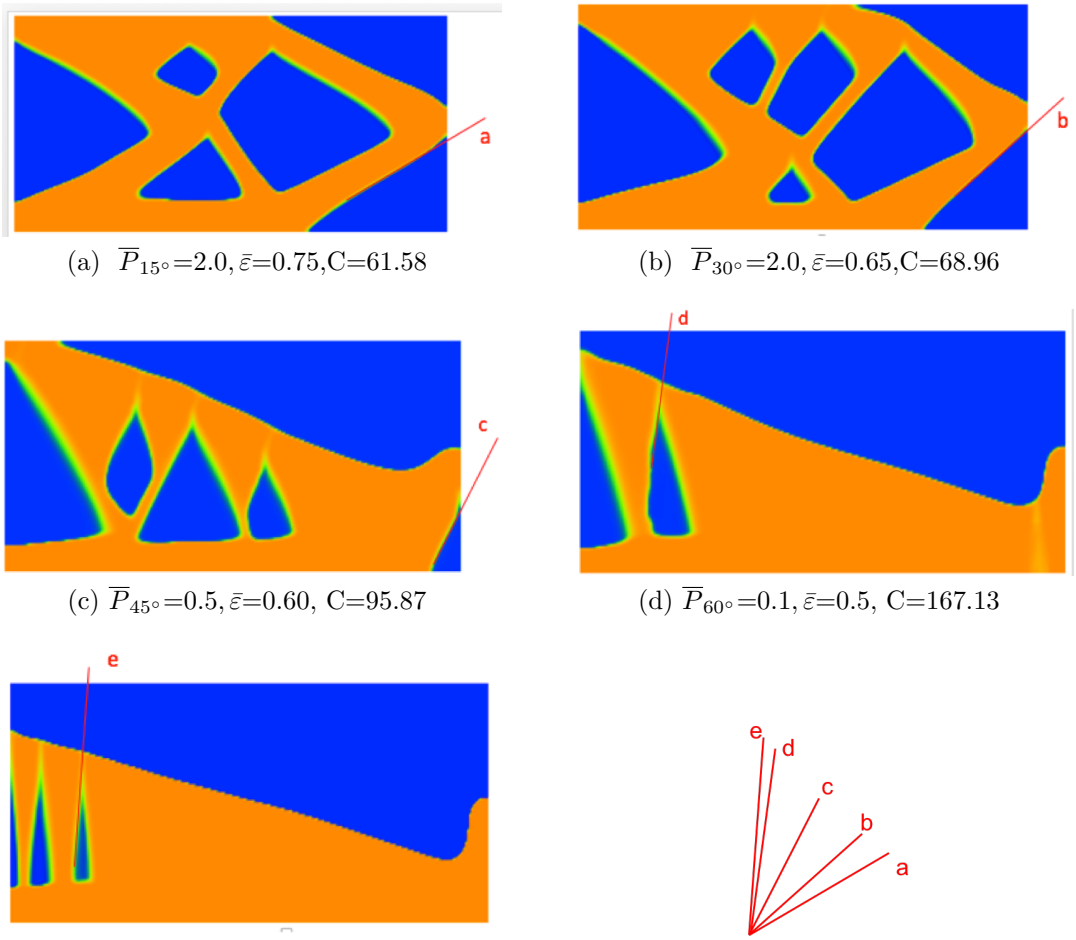

(a) $\overline{P}_{15^\circ}$=2.0, $\bar{\varepsilon}$=0.75,C=61.58

(b) $\overline{P}_{30^\circ}$=2.0, $\bar{\varepsilon}$=0.65,C=68.96

(c) $\overline{P}_{45^\circ}$=0.5, $\bar{\varepsilon}$=0.60, C=95.87

(d) $\overline{P}_{60^\circ}$=0.1, $\bar{\varepsilon}$=0.5, C=167.13

(e) $\overline{P}_{75^\circ}$=0.1, $\bar{\varepsilon}$=0.5,C=178.76

(f) Overlay of minimal overhang lines

Figure 13: Optimized cantilevers under different overhang angle $\bar{\alpha}$ constraint.

Figure 13 shows a set of optimized designs obtained under different overhang angle constraints $\bar{\alpha}$, with $\bar{\alpha}$ ranging from 15° to 75°. Also listed are the allowed projected perimeter length $\overline{P}_{\bar{\alpha}}$ and grayness threshold $\bar{\varepsilon}$ for each design and the corresponding compliance value for the optimized design. As the overhang angle $\bar{\alpha}$ increases from 15° to 75°, the compliance of the optimized design increases from 61.58 to 178.76. As a reference, the compliance for the optimized design without any overhang angle constraint is 58.11. In each subfigure of Fig. 13, a tangent line is drawn at the boundary point with minimal overhang angle. As

$\bar{\alpha}$ increases, the minimal slope of the boundary in these designs becomes higher and the minimal overhang angle in these designs increases from Figure 13(a) to (e), as seen in their overlay in Figure 13(f). It can also be seen that in all cases the minimal overhang angle is larger than the corresponding $\bar{\alpha}$ in each design. This example demonstrates that the proposed formulation is effective in controlling the minimal overhang angle in the optimized designs.

It should be noted that different projected perimeter $\overline{P}_{\bar{\alpha}}$ and grayness threshold $\bar{\varepsilon}$ are used for each design. As a general rule, we have found that, as the overhang angle $\bar{\alpha}$ becomes larger, smaller projected perimeter $\overline{P}_{\bar{\alpha}}$ and smaller grayness threshold $\bar{\varepsilon}$ are desirable. This is because, as the overhang angle constraint becomes tighter, large projected perimeters $\overline{P}_{\bar{\alpha}}$ would more likely to lead to the violation of overhang angle constraint. With the tighter angle constraint, intermediate density is also more likely to appear in the optimized design. Thus, the grayness threshold $\bar{\varepsilon}$ needs to be set smaller. In all cases, the projected perimeter constraints are active in the optimized designs. The grayness constraints are initially active and useful for controlling the optimized designs. However, they become inactive later when the effect of the Heaviside filter becomes more dominant as β_d becomes larger.

(a) W/O side perimeter constraint, C=68.91

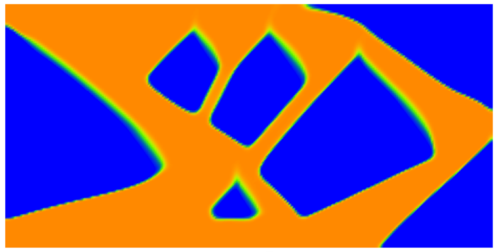

(b) W/ $\bar{P}_{\mathbf{side}} = 0.3$, C=68.96

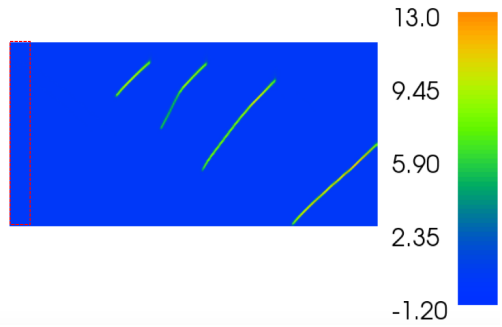

(c) $H(\mathbf{b}\cdot\nabla\bar{\tilde{\gamma}})H(\mathbf{n}_{\mathrm{L}}\cdot\nabla\bar{\tilde{\gamma}})\mathbf{b}\cdot\nabla\bar{\tilde{\gamma}}$

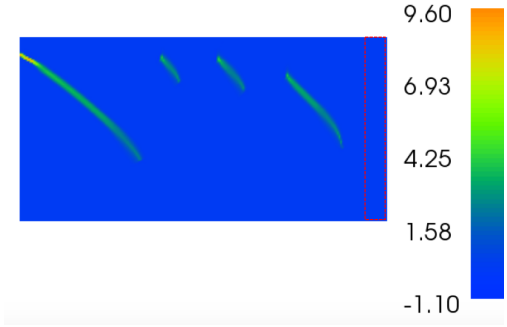

(d) $H(\mathbf{b}\cdot\nabla\bar{\tilde{\gamma}})H(\mathbf{n}_{\mathrm{R}}\cdot\nabla\bar{\tilde{\gamma}})\mathbf{b}\cdot\nabla\bar{\tilde{\gamma}}$

Figure 14: Optimized designs without and with side perimeter constraint under overhang angle constraint $\bar{\alpha} = 30°$.

In all the above designs, due to the imposing of side perimeter constraint (12) with $\bar{P}_{\mathbf{side}} = 0.3$, there are no side features that require support. Figure 14 compares two designs without and with the side projected perimeter constraint (12). These designs are obtained

with minimal overhang angle constraint $\bar{\alpha} = 30°$. These two designs have nearly identical compliance. Without the side perimeter constraint as shown in Fig. 14(a), the left boundary has a feature requiring support. With the constraint, the design Fig. 14(b) is free from such features. Figure 14(c) and (d) show the distribution of left side zone and right side zone based Heaviside projected directional gradient for the design in Fig. 14(c). It is clear that there is no visible directional gradient in the left side zone inFig. 14(c) or in the right side zone in Fig. 14(d). When compared with Fig. 5(b) and (c), this example illustrates that the side perimeter constraint is effective in preventing boundary induced undercut requiring support.

5.3.2 Discussions

In this subsection, we take the above optimal design of cantilever beams as an example to discuss our formulation for overhang angle control.

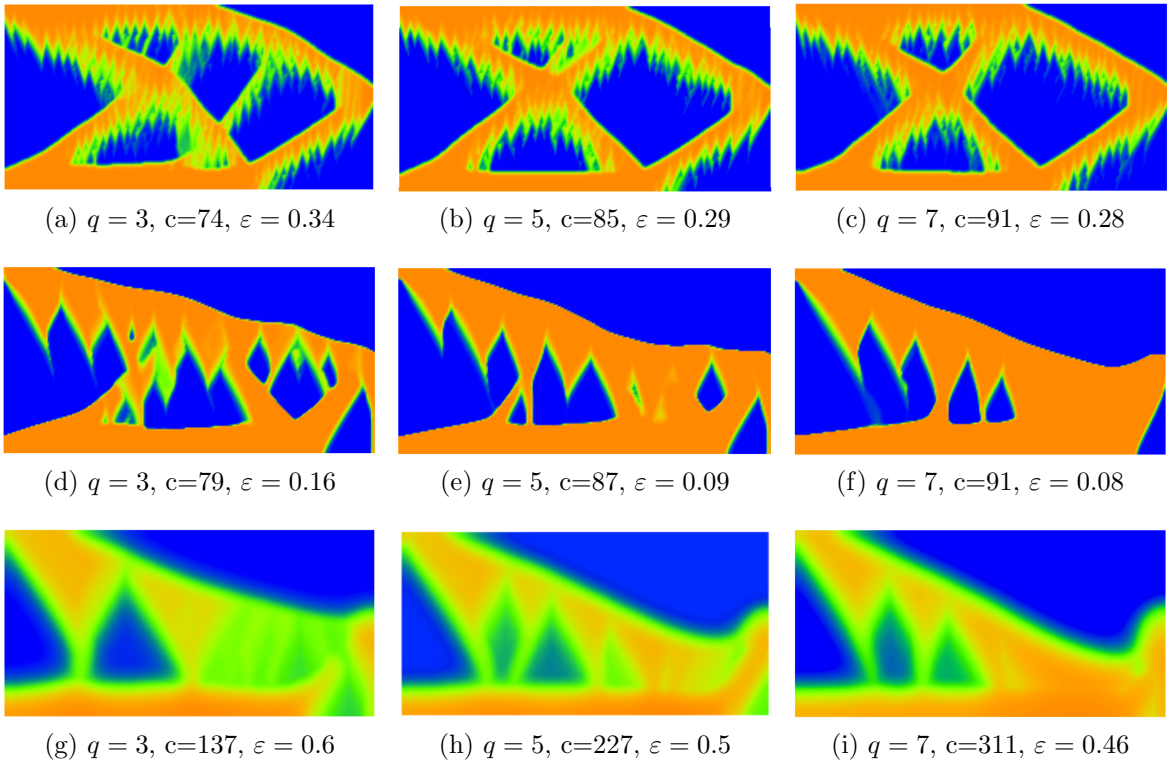

(a) $q = 3$, c=74, $\varepsilon = 0.34$ (b) $q = 5$, c=85, $\varepsilon = 0.29$ (c) $q = 7$, c=91, $\varepsilon = 0.28$

(d) $q = 3$, c=79, $\varepsilon = 0.16$ (e) $q = 5$, c=87, $\varepsilon = 0.09$ (f) $q = 7$, c=91, $\varepsilon = 0.08$

(g) $q = 3$, c=137, $\varepsilon = 0.6$ (h) $q = 5$, c=227, $\varepsilon = 0.5$ (i) $q = 7$, c=311, $\varepsilon = 0.46$

Figure 15: The effect of the SIMP penalty coefficient q and filter size r_f on optimized designs. In all designs, allowed grayness constraint $\bar{\varepsilon} = 0.6$. The designs in the top row are obtained with filter radius $r_f = 3$, 2nd row with $r_f = 15$ and the bottom with $r_f = 25$.

Due to the incorporation of the overhang angle constraint (8d) in the optimization formulation, the resulting optimized designs exhibit boundary oscillation if we do not impose grayness constraint (8e) or density Heaviside filter. Figure 15 illustrates the optimized de-

signs under different SIMP penalty coefficient q and different filter size r_f. These designs are obtained under overhang angle constraint $\bar{\alpha} = 45$ and projected perimeter constraint $\overline{P}_{45^\circ} = 0.5$. In all the designs, the grayness constraint $\bar{\varepsilon} = 0.6$ is imposed. In the top row are designs obtained with filter size $r_f = 3$, the 2nd row with $r_f = 15$ and the bottom with $r_f = 25$. As can be seen, as the penalty q increases from 3 to 7, the grayness ε in the resulting design reduces in all three rows, respectively. When $f_r = 3$, the resulting designs for all q have relatively clear density contrast except at the overhang boundary where boundary oscillation occurs due to the overhang angle constraint (8d). The reason for such oscillated boundary in the top row in Fig. 15 is that the optimizer leads to design with oscillating boundary in order to meet the overhang angle constraint (8d) and the FE mesh is not dense enough for accurately analyzing such sharp boundary change. We thus choose to use larger filter size to ensure that the FE analysis is sufficiently accurate for the underlying feature. When the filter size is increased to 15 in the 2nd row, the high-frequency oscillation has faded. When the filter size is increased to 25, there is no oscillation since the underlying feature size is sufficiently large for the FE analysis and an oscillating boundary shape no longer represents an economic distribution of material for minimizing the compliance. When $f_r = 25$ (the bottom row), the resulting designs are free from boundary oscillation, but all have relatively high grayness, regardless of q value. However, larger penalty q, e.g. $q = 5$ or 7, does lead to clearer contour than at $q = 3$. Note that, in this paper, the penalty $q = 5$ is chosen in all other cases. Due to the use of larger filter size to overcome boundary oscillation, high grayness exists in the optimized designs even with high SIMP penalty q. Therefore, additional measures are needed to suppress the high grayness.

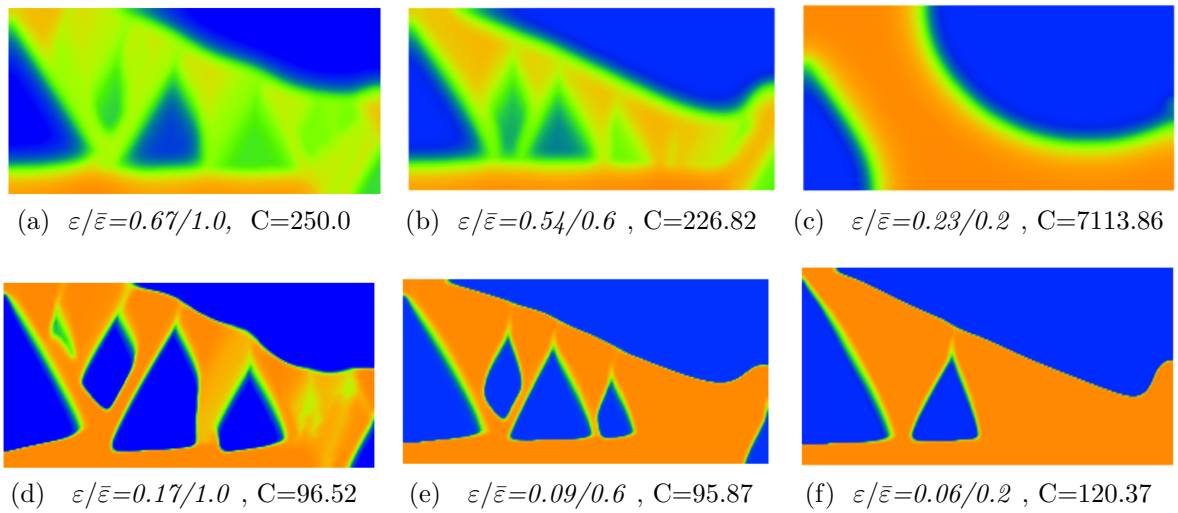

(a) $\varepsilon/\bar{\varepsilon}$=*0.67/1.0,* C=250.0 (b) $\varepsilon/\bar{\varepsilon}$=*0.54/0.6* , C=226.82 (c) $\varepsilon/\bar{\varepsilon}$=*0.23/0.2* , C=7113.86

(d) $\varepsilon/\bar{\varepsilon}$=*0.17/1.0* , C=96.52 (e) $\varepsilon/\bar{\varepsilon}$=*0.09/0.6* , C=95.87 (f) $\varepsilon/\bar{\varepsilon}$=*0.06/0.2* , C=120.37

Figure 16: The effect of grayness constraint and/or the density Heaviside filter in suppressing intermediate density. $\bar{\alpha} = 45^\circ$ and $P_{45^\circ} = 0.5$.

In order to suppress grayness in the optimized designs, in this paper, we use the density Heaviside filtering and grayness constraints. We first compare the optimized designs with

and without density Heaviside filtering and under different grayness constraints in Fig. 16. The grayness ε in the converged designs and the grayness constraint $\bar{\varepsilon}$ are noted as $\varepsilon/\bar{\varepsilon}$. These designs are obtained under overhang angle constraint $\bar{\alpha} = 45$ and projected perimeter constraint $\overline{P}_{45^\circ} = 0.5$. In the top row of Fig. 16 are designs obtained without density Heaviside filtering with grayness constraint $\bar{\varepsilon}$ ranges from 1.0, to 0.6 and 0.2. It should be noted that when $\bar{\varepsilon} = 1.0$, it effectively means there is no grayness constraint since the maximum possible ε is 1. As can be seen, as $\bar{\varepsilon}$ becomes tighter, the resulting design exhibits clearer contrast, but also with simpler topology. That is, *the combination of larger filter size to suppress boundary oscillation and tighter grayness constraint to suppress intermediate density leads to resulting designs of much simpler topology* as shown in Fig. 16(c). It has quite large compliance (7113.86), thus not a desirable design. Thus the grayness constraint alone is not sufficient for obtaining designs with good compliance, clear contrast and free-form boundary oscillation.

In the bottom row of Fig. 16, the density Heaviside filtering is used in addition to the grayness constraint. Comparing the designs between the top row and the bottom row, it is clear that the density Heaviside filtering is useful for suppressing the high intermediate density. However, when there is no grayness constraint at all as in Fig. 16(d), the resulting design still has somewhat gray regions. That is, the density Heaviside filtering alone is not sufficient for ensuring that the resulting design has clear density contrast. The next example further illustrates this.

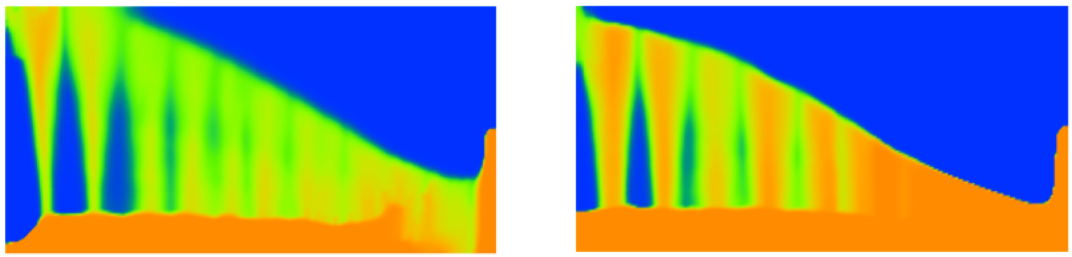

(a) $\bar{\varepsilon}$=1.0, $P = 0.696$, C=314.11

(b) $\bar{\varepsilon}$=0.8, $P = 0.314$, C=239.02

(c) $\bar{\varepsilon}$=0.7, $P = 0.100$, C=183.55

(d) $\bar{\varepsilon}$=0.6, $P = 0.100$, C=184.10

Figure 17: The combination of the density Heaviside filter and the grayness constraint is effective in suppressing the intermediate density. In this example, the overhang angle constraint $\bar{\alpha} = 75^\circ$ and $\bar{P}_{75^\circ} = 0.1$. The maximum $\beta_d^{\max}$ is 128 in all cases.

When the overhang angle constraint becomes very tight, i.e. overhang angle becomes

very large, the density Heaviside filter alone is not sufficient for obtaining designs meeting the overhang angle constraint and with clear density contrast. Figure 17 displays optimized designs obtained with the density Heaviside filtering under different grayness constraint. In this figure, all designs are obtained under the overhang angle constraint $\bar{\alpha} = 75^\circ$ and the projected perimeter constraint $\bar{P}_{75^\circ} = 0.1$. All designs are obtained under the density Heaviside filtering. In order to obtain the maximally possible clear designs, the control parameter of the density Heaviside filter is set to $\beta_d^{\max} = 128$. When the grayness constraint $\bar{\varepsilon}$ is set 1.0 and 0.8 as shown in Fig. 17(a) and (b), despite the large $\beta_d^{\max}$ value, the resulting designs still exhibit significant intermediate density and the projected perimeter constraints are not satisfied with P equaling to 0.696 and 0.314, exceeding the allowed $\overline{P}_{75^\circ} = 0.1$. These two designs suggest that the density Heaviside filter along is insufficient to obtain designs with clear contrast. In fact, the resulting designs before the Heaviside filtering have density mostly equal to $\eta = 0.5$. Thus, even with the Heaviside filter, the resulting designs exhibit strong intermediate density with $\gamma = 0.5$. When the grayness constraint becomes tighter with $\bar{\varepsilon} = 0.7$ and 0.6 as shown in Fig. 17(c) and (d), it moderates the topology and leads to optimized designs with fewer holes. The resulting designs exhibit clear contrast and satisfy the projected perimeter constraint. This example thus demonstrates that *the grayness constraint is useful for controlling the topology in the optimized design and its combination with the density Heaviside filter is effective for obtaining good designs with clear density contrast for minimal overhang angle control.*

In summary, the overhang angle constraint (8d) could lead to boundary oscillation. A larger filter size can then be used to suppress such boundary oscillation. As such, it leads to high grayness in the resulting designs, if without explicit grayness control. The combination of the grayness constraint and the density Heaviside filtering is particularly effective for suppressing the high intermediate density. The grayness constraint also has the effect of moderating the topology of the resulting designs. It should be noted that, in the undercut control (4d), there is no boundary oscillation. Thus, there is no need for relatively large filter size. The grayness constraint alone is sufficient to suppress potential excessive intermediate density in the optimized designs.

5.3.3 Minimal overhang angle control for heat conduction

We have extended this minimal overhang angle control method to the heat conduction problems. Figure 18 shows a set of optimized material distributions for minimizing thermal compliance. The domain size is 8×8. The Dirichlet boundary condition (zero temperature) is prescribed at the middle of the bottom edge spanning 20% of the edge length. The thermal conductivity is $E = 1.0$ for the solid material and $E_{\min}$ =1e-3 for void. There are 51,200 triangular elements and 25,921 nodes (optimization variables). For all designs in Fig. 18, filter radius r_f is 25 and the volume fraction 0.4. The termination criteria is maximum 400 iterations or maximum change of density 0.01. The allowed projected perimeter $\overline{P}_\alpha$ is 0.1 and allowed grayness threshold $\bar{\varepsilon}$ is 0.2 in all cases. The grayness constraint starts at 1.0 and decreases by 1.5 times every 25 iterations until it reaches 0.2. The β_d in the density Heaviside filter starts at 1 and, from iteration 49, increases every 25 iterations by 1.5 times

(a) No $\bar{\alpha}$ constraint. C=6.537e3

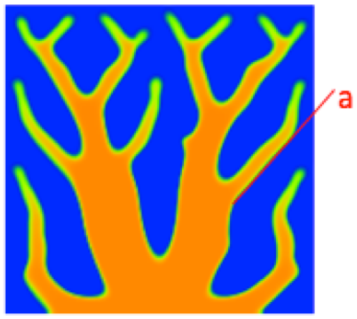

(b) $\bar{\alpha} = 15°$, C=7.478e3

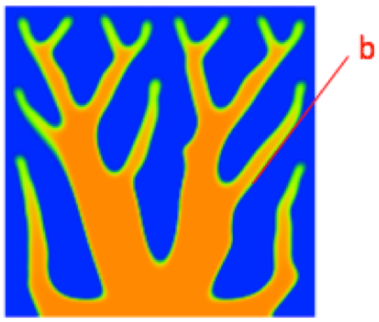

(c) $\bar{\alpha} = 30°$, C=7.505e3

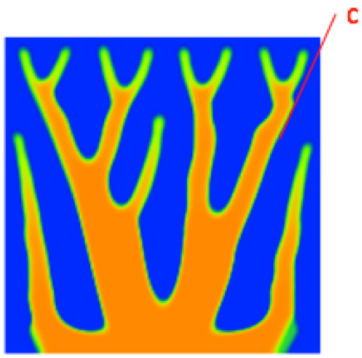

(d) $\bar{\alpha} = 45°$, C=7.524e3

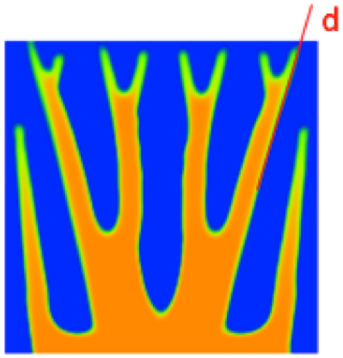

(e) $\bar{\alpha} = 60°$, C=7.722e3

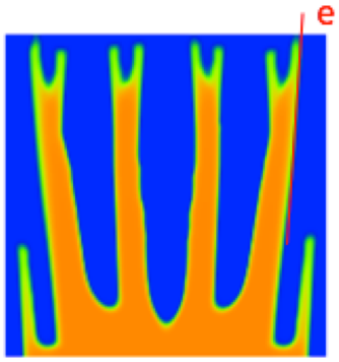

(f) $\bar{\alpha} = 75°$, C=8.824e3

(g) Overlay of minimal overhang lines

Figure 18: Optimized material distributions for minimizing thermal compliance under different minimal overhang angle constraints $\bar{\alpha}$.

until it reaches $\beta_d^{\max} = 32$. The β for the Heaviside projection of directional gradient in (1) is 10.

Figure 18(a) shows the optimized design without overhang angle constraint and the resulting compliance is 6.537e3. Figure 18(b) to (f) show the optimized designs under overhang angle constraints with $\bar{\alpha}$ increasing from 15° to 75°. The corresponding compliance values also increase from 7.748e3 to 8.824e3. The tangent lines at points with minimal overhang angles are highlighted in each subfigure and overlaid in Fig. 18(g). This example demonstrates that this method is effective in controlling the minimal overhang angle in the optimized designs.

We have also extended the method to three-dimensional heat conduction problems. The design domain is $4 \times 4 \times 4$. There are 3,072,000 tetrahedral elements of 531,441 nodes (optimization variables). The Dirichlet boundary condition (zero temperature) is prescribed at the middle of the bottom face spanning 20% × 20% of the face size. The filter size is $r_f = 10$ unless otherwise specified. The β for the Heaviside projection of directional gradient in (1) is 10. All examples are obtained with projected perimeter constraint $P_{\bar{\alpha}} = 0.1$. The grayness threshold $\bar{\varepsilon}$ starts with 1 and decreases to 0.2 at the rate of 1.25 times for every 25 iterations. The density Heaviside filter β_d starting at 1.0, increases from iteration 48, at the rate of 1.5 every 25 iterations until $\beta_d^{\max} = 16$. The optimization termination criteria is maximum 400 iterations or the maximum change of density 0.01. The volume fraction of the solid material is 0.3.

Figure 19 shows the optimized 3D designs under different overhang angle $\bar{\alpha}$ constraints ranging from 15° to 75°. In each subfigure, there are two views, an isometric and a cross-sectional view, of the same design. As can be seen in Fig. 19(e), when $\bar{\alpha} = 75$, the resulting design is nearly straight from the top to bottom. When viewed from the top, the top surface is nearly of the same size as the bottom and thus one can directly see through to the bottom for a large portion of the design. On the other hand, for $\bar{\alpha} = 15$ as shown in Fig. 19(a), the top surface occupies a big portion of the domain and there is very little space from which one can see through to the bottom. For all designs obtained with overhang angles between 15° and 75°, the areas of top surfaces gradually become smaller and the branches are connected only at the bottom to accommodate the increasing overhang angle constraints. In order to better visualize the change of the overhang angles, we draw the tangent line at the boundary point with minimal overhang angle in each cross-sectional view. Comparing these tangent lines illustrates that the resulting 3D designs exhibit clear overhang angle control. For designs under overhang angle constraint $\bar{\alpha}$ at 45° and 60°, the cross-sectional views also exhibit overhang bridge highlighted in ellipses in Fig. 19(c) and (d). Comparing the two overhang bridges, it can be seen that the bridge from the overhang angle 60° has steeper slope than the design from 45°. This thus again illustrates that the overhang angle control is effective. It is also worth noting that, unlike previous examples, the increase of overhang angle $\bar{\alpha}$ does not lead to the increase of the thermal compliance. This can be ascribed to the fact that multiple local minimums exist in the proposed optimization problem.

The filter size r_f in all designs in is 10 except the design in Fig. 19(a) and (b), corresponding to overhang angle constraint $\bar{\alpha}$= 15° and 30°. In these two designs, the filter size

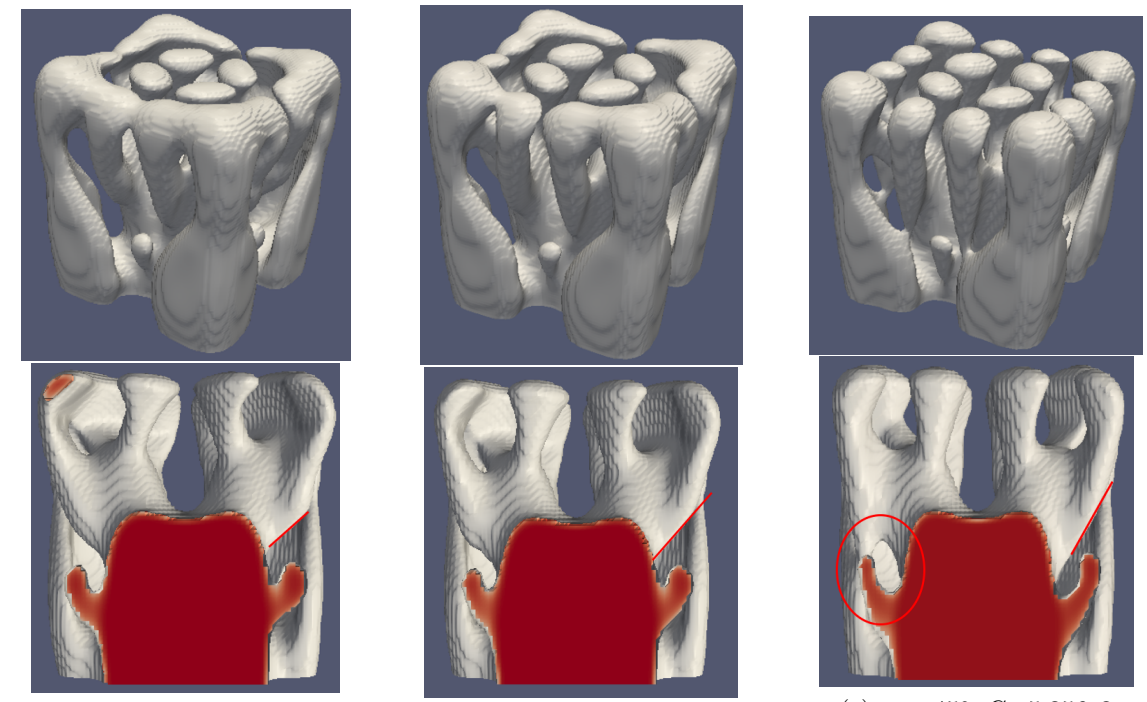

(a) $\bar{\alpha} = 15°$, r_f=11, C=5.590e3 (b) $\bar{\alpha} = 30°$, r_f=11, C=5.584e3 (c) $\bar{\alpha} = 45°$, C=5.356e3

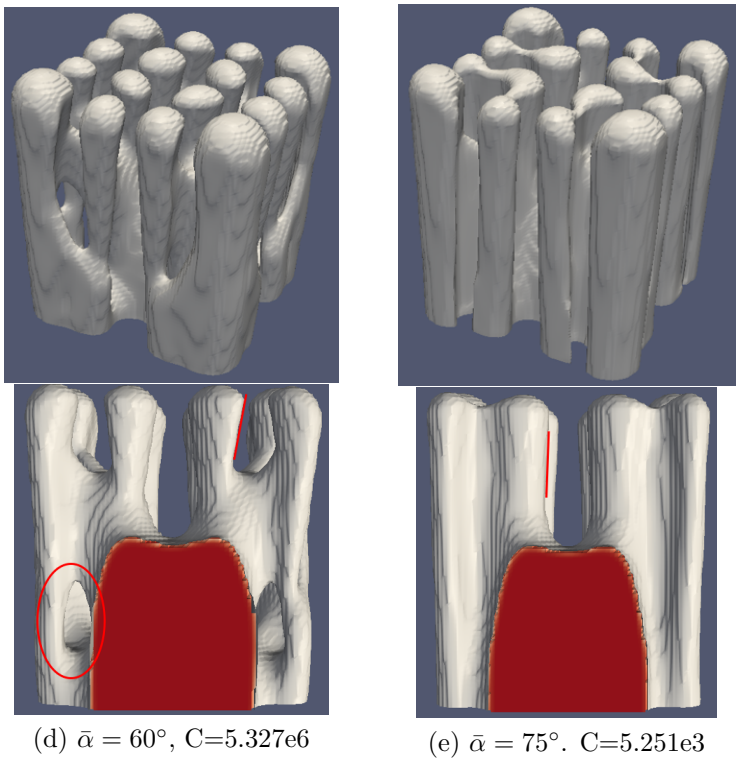

(d) $\bar{\alpha} = 60°$, C=5.327e6 (e) $\bar{\alpha} = 75°$. C=5.251e3

Figure 19: Optimized 3D designs for heat conduction under different overhang angle $\bar{\alpha}$ constraint.

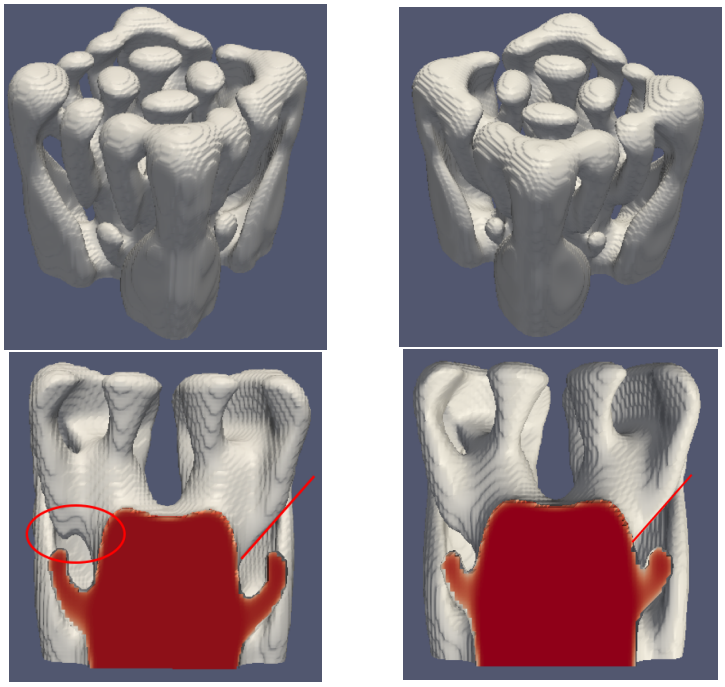

(a) $\bar{\alpha} = 30°$, r_f=10, C=5.415e3 (b) $\bar{\alpha} = 30°$, r_f=11, C=5.584e3

Figure 20: The increase of filter size r_f is beneficial in suppressing boundary oscillation.

is $r_f = 11$. The reason for the increase of filter size is that smaller filter size at $r_f = 10$ leads to boundary oscillation. The increase to $r_f = 11$ overcomes the oscillation. This change of boundary oscillation is shown in Fig. 20 for overhang angle constraint $\bar{\alpha}$= 30°. The oscillation in Fig. 20(a) is highlighted. This increase of filter size to suppress boundary oscillation is similar to the effect observed in the cantilever example in Fig. **??**.

5.3.4 Experimental build

In order to experimentally verify that the minimal overhang angle constrained designs can indeed be built without the support structure, the design corresponding to Fig. 19(c) with minimal overhang angle $\bar{\alpha} = 45°$ is built on two fused deposition modeling (FDM) machines. First it was built on a Stratasys Dimension Elite with the support structure. Figure 21(a) shows the built part before the support structure was removed. Fig. 21(b) displays the part after the support was removed. This part volume is 1.42 in^3 and the support volume is 1.26 in^3. That is, the fabrication of this part takes additional 89% of material volume in support structure. The design was also built on a second machine, XYZ da Vinci 2.0, without any support. Fig. 21(c) shows the printed part in the machine where there is no support and Fig. 21(d) displays a zoom-in view of the built part. This example demonstrate that the proposed overhang based PUP formulation can indeed lead to optimized designs that can be built without any support structures.

(a) W/ support on Dimension Elite

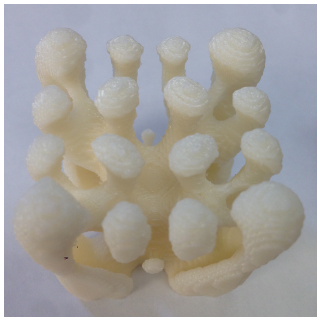

(b) Top view

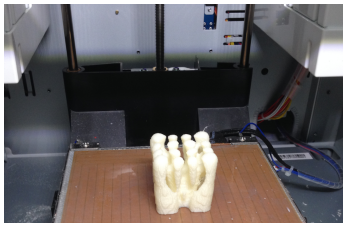

(c) W/O support on XYZ da Vinci 2.0 Duo

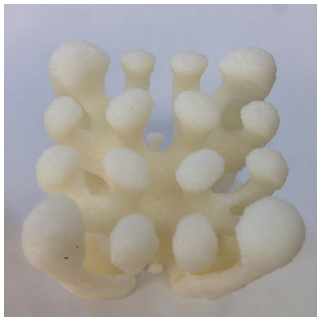

(d) Top view

Figure 21: Building the optimized design (Fig. 19(c)) on FDM machines with and without the support.

6 Conclusions and discussions

This paper presents two formulations for controlling the undercut and for controlling the minimal overhang angle in density based topology optimization. In both formulations, the constraints are cast into the HPI form with explicit geometric meanings. For undercut control, this integral form corresponds to projected undercut perimeter. For overhang angle control, this corresponds to projected perimeter with slope smaller than the prescribed overhang angle. In both formulations, in addition to the projected perimeter constraints, a constraint on intermediate density is necessary to obtain designs of clear contrast. For overhang angle control, density Heaviside filtering is also needed. In order to avoid requiring support structure in the boundary, a side zone based projected perimeter constraint is also imposed. Various numerical experiments, including both 2D and 3D examples of minimal compliance and minimal thermal compliance, have been conducted. They demonstrate that the proposed formulations based on the combination of the integral form of projected perimeter constraint and the density grayness constraint are effective for undercut control and for minimal overhang angle control.

Our numerical experiments have led to the following observations.

1. When the allowed projected perimeter approaches zero, the resulting design always satisfies the undercut constraint or the minimal overhang angle constraint. On the other hand a larger allowed projected perimeter can usually lead to designs of more complex topology with better compliance since HPI formulations are conservative. However, overly large allowed projected perimeter runs the risk of violating undercut constraint or the minimal overhang angle constraint.

2. The grayness constraint has the effect of suppressing intermediate density. It also regulates the topology (the number of holes). Smaller grayness value allows fewer holes. On the other hand, larger grayness can lead to overly gray structures. This is especially true when projected perimeter becomes tight and near-uniform intermediate density tends to appear.

3. It is difficult to use the density Heaviside filter alone to avoid intermediate density. This occurs especially when projected perimeter constraint is very tight. In order to satisfy the projected perimeter constraint, intermediate density with $\gamma = \eta = 0.5$ appears. Thus, the grayness constraint is needed to suppress intermediate density.

4. Boundary oscillation may occur in minimal overhang angle control and relatively larger filter size is needed to suppress such oscillation. The combination of large filter size and tight grayness constraint can lead to poor designs consisting of overly large features. The density Heaviside filter becomes effective and necessary in obtaining better designs of smaller features with clean contrast. An alternative to large filter radius for minimal overhang angle control would be to use finer meshes for FE analysis than for density representation.

Our study has also revealed one especially interesting finding, that is, accounting for support structures in topology optimization can, in some 3D cases, lead to designs with better performance.

Although the combination of HPI based projected perimeter constraint and the grayness constraint are effective for controlling the undercut and for controlling the minimal overhang angle, the precise perimeter and grayness threshold for obtaining a good design with clear density contrast still require some tuning. Thus future work would study how to automatically specify the parameters such as the allowed perimeter constraint, grayness constraint and filter radius. Future work would also study how the proposed formulations might be applicable to other manufacturability constraints in topology optimization.

Acknowledgement

The author wants to acknowledge the support from the National Science Foundation grants 1404665, 1435072 and 1561917, an unrestricted grant from GE Global Research and the UW-Madison Technology Innovation Fund.

References

[1] M.P. Bendsoe and N. Kikuchi. Generating optimal topologies in structural design using a homogenization method. *Computer Methods in Applied Mechanics and Engineering*, 71(2):197–224, 1988.

[2] M.P. Bendsøe and O. Sigmund. *Topology Optimization: Theory, Methods, and Applications*. Springer Verlag, 2003.

[3] Joshua D Deaton and Ramana V Grandhi. A survey of structural and multidisciplinary continuum topology optimization: post 2000. *Structural and Multidisciplinary Optimization*, 49(1):1–38, 2014.

[4] Martin P Bendsøe. Optimal shape design as a material distribution problem. *Structural optimization*, 1(4):193–202, 1989.

[5] M Zhou and GIN Rozvany. The coc algorithm, part ii: topological, geometrical and generalized shape optimization. *Computer Methods in Applied Mechanics and Engineering*, 89(1):309–336, 1991.

[6] HP Mlejnek. Some aspects of the genesis of structures. *Structural Optimization*, 5(1-2):64–69, 1992.

[7] Grégoire Allaire, François Jouve, and Anca-Maria Toader. Structural optimization using sensitivity analysis and a level-set method. *Journal of computational physics*, 194(1):363–393, 2004.

[8] Michael Yu Wang, Xiaoming Wang, and Dongming Guo. A level set method for structural topology optimization. *Computer methods in applied mechanics and engineering*, 192(1):227–246, 2003.

[9] J Sokolowski and A Zochowski. On the topological derivative in shape optimization. *SIAM Journal on Control and Optimization*, 37(4):1251–1272, 1999.

[10] Krishnan Suresh. Efficient generation of large-scale pareto-optimal topologies. *Structural and Multidisciplinary Optimization*, 47(1):49–61, 2013.

[11] Blaise Bourdin and Antonin Chambolle. Design-dependent loads in topology optimization. *ESAIM: Control, Optimisation and Calculus of Variations*, 9:19–48, 2003.

[12] YM Xie and Grant P Steven. A simple evolutionary procedure for structural optimization. *Computers & structures*, 49(5):885–896, 1993.

[13] Ming Zhou, Raphael Fleury, Yaw-Kang Shyy, Harold Thomas, and JM Brennan. Progress in topology optimization with manufacturing constraints. In *Proceedings of the 9th AIAA MDO conference AIAA-2002-4901*, 2002.

[14] Allan Roulund Gersborg and Casper Schousboe Andreasen. An explicit parameterization for casting constraints in gradient driven topology optimization. *Structural and Multidisciplinary Optimization*, 44(6):875–881, 2011.

[15] James K Guest and Mu Zhu. Casting and milling restrictions in topology optimization via projection-based algorithms. In *ASME 2012 International Design Engineering Technical Conferences and Computers and Information in Engineering Conference*, pages 913–920. American Society of Mechanical Engineers, 2012.

[16] Qi Xia, Tielin Shi, Michael Yu Wang, and Shiyuan Liu. A level set based method for the optimization of cast part. *Structural and Multidisciplinary Optimization*, 41(5):735–747, 2010.

[17] Qi Xia, Tielin Shi, Michael Yu Wang, and Shiyuan Liu. Simultaneous optimization of cast part and parting direction using level set method. *Structural and Multidisciplinary Optimization*, 44(6):751–759, 2011.

[18] Thomas A Poulsen. A new scheme for imposing a minimum length scale in topology optimization. *International Journal for Numerical Methods in Engineering*, 57(6):741–760, 2003.

[19] JK Guest, JH Prévost, and T. Belytschko. Achieving minimum length scale in topology optimization using nodal design variables and projection functions. *International Journal for Numerical Methods in Engineering*, 61(2):238–254, 2004.

[20] F. Wang, B.S. Lazarov, and O. Sigmund. On projection methods, convergence and robust formulations in topology optimization. *Structural and Multidisciplinary Optimization*, 43:767– 784, 2011.

[21] X. Qian and O. Sigmund. Topological design of electromechanical actuators with robustness toward over-and under-etching. *Computer Methods in Applied Mechanics and Engineering*, 253:237–251, 2012.

[22] Mingdong Zhou, Boyan S Lazarov, Fengwen Wang, and Ole Sigmund. Minimum length scale in topology optimization by geometric constraints. *Computer Methods in Applied Mechanics and Engineering*, 293:266–282, 2015.

[23] James K Guest. Imposing maximum length scale in topology optimization. *Structural and Multidisciplinary Optimization*, 37(5):463–473, 2009.

[24] Yiqiang Wang, Lei Zhang, and Michael Yu Wang. Length scale control for structural optimization by level sets. *Computer Methods in Applied Mechanics and Engineering*, 305:891–909, 2016.

[25] Grégoire Allaire, François Jouve, and Georgios Michailidis. Thickness control in structural optimization via a level set method. *Structural and Multidisciplinary Optimization*, 53(6):1349–1382, 2016.

[26] Alireza Asadpoure, James K Guest, and Lorenzo Valdevit. Incorporating fabrication cost into topology optimization of discrete structures and lattices. *Structural and Multidisciplinary Optimization*, 51(2):385–396, 2014.

[27] D Brackett, I Ashcroft, and R Hague. Topology optimization for additive manufacturing. In *Proceedings of the Solid Freeform Fabrication Symposium, Austin, TX*, pages 348–362, 2011.

[28] Andrew T Gaynor and James K Guest. Topology optimization for additive manufacturing: considering maximum overhang constraint. In *15th AIAA/ISSMO multidisciplinary analysis and optimization conference*, pages 16–20, 2014.

[29] Andrew T Gaynor and James K Guest. Topology optimization considering overhang constraints: Eliminating sacrificial support material in additive manufacturing through design. *Structural and Multidisciplinary Optimization*, pages 1–16, 2016.

[30] Matthijs Langelaar. Topology optimization of 3d self-supporting structures for additive manufacturing. *Additive Manufacturing*, 12, Part A:60 – 70, 2016.

[31] Amir M Mirzendehdel and Krishnan Suresh. Support structure constrained topology optimization for additive manufacturing. *Computer-Aided Design*, 2016.

[32] Atsushi Kawamoto, Tadayoshi Matsumori, Shintaro Yamasaki, Tsuyoshi Nomura, Tsuguo Kondoh, and Shinji Nishiwaki. Heaviside projection based topology optimization by a PDE-filtered scalar function. *Structural and Multidisciplinary Optimization*, 44(1):19–24, 2011.

[33] B. S. Lazarov and O. Sigmund. Filters in topology optimization based on Helmholtz-type differential equations. *International Journal for Numerical Methods in Engineering*, 86(6):765–781, 2011.

[34] Xiaoping Qian and Ercan M. Dede. Topology optimization of a coupled thermal-fluid system under a tangential thermal gradient constraint. *Structural and Multidisciplinary Optimization*, 54(3):531–551, 2016.

[35] Shengli Xu, Yuanwu Cai, and Gengdong Cheng. Volume preserving nonlinear density filter based on heaviside functions. *Structural and Multidisciplinary Optimization*, 41(4):495–505, 2010.

[36] Anders Logg, Kent-Andre Mardal, and Garth Wells. *Automated solution of differential equations by the finite element method: The FEniCS book*, volume 84. Springer Science & Business Media, 2012.

[37] K. Svanberg. The method of moving asymptotes: A new method for structural optimization. *International Journal of Numerical Methods in Engineering*, 24:359 – 373, 1987.

[38] Joakim Petersson. Some convergence results in perimeter-controlled topology optimization. *Computer Methods in Applied Mechanics and Engineering*, 171(1):123–140, 1999.

[39] Joakim Petersson, Muriel Beckers, and Pierre Duysinx. Almost isotropic perimeters in topology optimization: Theoretical and numerical aspects. In *Third World Congress of Structural and Multidisciplinary Optimization*, 1999.

[40] Xiaoping Qian. Topology optimization in B-spline space. *Computer Methods in Applied Mechanics and Engineering*, 265:15–35, 2013.